



Dynamics of single, non-spherical ellipsoidal particles in a turbulent channel flow

D.O. Njobuenwu*, M. Fairweather

Institute of Particle Science and Engineering, School Chemical and Process Engineering, University of Leeds, Leeds LS2 9JT, UK



HIGHLIGHTS

- Eulerian–Lagrangian with Euler rotational equation represents particle dynamics.
- Technique developed is applicable to any regular isotropic non-spherical particle.
- Ellipsoidal particles display a transition from one orientational state to another.
- Particle orientation is affected by the shear rate, particle inertia and shape.

ARTICLE INFO

Article history:

Received 10 July 2014

Received in revised form

3 November 2014

Accepted 8 November 2014

Available online 18 November 2014

Keywords:

Channel flow

Large eddy simulation

Lagrangian particle tracking

Non-spherical particles

Orientation

Turbulence

ABSTRACT

Using disk, spherical and needle-like particles with equal equivalent volume diameters, the orientational dynamics of non-spherical particles is studied in a turbulent channel flow. An Eulerian–Lagrangian approach based on large eddy simulation with a dynamic sub-grid scale model is used to predict a fully developed gas–solid flow at a shear Reynolds number $Re_\tau=300$. Particle shape and orientation are accounted for by the coupling between Newton's law of translational motion and Euler's law of rotational motion, both in a Lagrangian framework. The particle shapes are simulated using the super-quadrics form, with the dynamically relevant parameters being the particle aspect ratio, equivalent volume diameter and response time. The translational and orientational behaviour of single particles initially released at three different locations in the wall-normal direction are monitored, with analysis showing a clear distinction between the behaviour of the different particle shapes. The results show that turbulent dispersion forces non-spherical particles to have a broad orientation distribution. The orientational states observed include periodic, steady rotation, tumbling, precessing and nutating. Velocity gradient, aspect ratio and particle inertia all have an effect on the alignment of the particle principal axis to the inertial axes. Unlike spherical particles, the disk and needle-like particles display a transition from one orientational state to another, especially when their initial position is in the near-wall region, with the frequency of this transition highest for the disk-like particle. Overall, this study leads to an improved understanding of the significance of shape on particle behaviour which is of relevance to many practical flows.

© 2014 Elsevier Ltd. All rights reserved.

1. Introduction

Non-spherical particles suspended in a wall-bounded turbulent flow display varying linear (position and velocity) and rotational (orientation and rotation) attributes under the action of the velocity gradient. Understanding these dynamic attributes is important in many areas of science and engineering, and in many practical applications. For example, their importance spans the fundamental

properties of turbulence and the rheological properties of suspensions, with relevant applications ranging from the deposition of aerosols in respiratory organs, the distribution of cellulose fibres in the paper and pulp industry, the motion of red blood cells travelling through blood vessels, and ice crystal dynamics in clouds, to name but a few. Of particular interest here are flows of relevance to nuclear reactor operations, where corrosion products can be transported into the reactor core by the cooling fluids, and in some cases are deposited on the outside of the fuel pins in the form of CRUD (an acronym for Chalk River unidentified deposit or corrosion residual unidentified deposit). Individual particles are small, of the order of 0.1–2.0 μm , but these agglomerate into larger particles giving rise to

* Corresponding author. Tel.: +44 113 343 2351.

E-mail address: d.o.njobuenwu@leeds.ac.uk (D.O. Njobuenwu).

a wide range of sizes and morphologies, varying from needle-like, through near-spherical to platelets or flakes (Hazelton, 1987). Particles suspended in a turbulent fluid undergo mean motion due to the mean fluid velocity and random motion due to the fluctuating component of that velocity. For non-spherical particles, their motion is then a combination of translation and rotation due to the anisotropy of their shape and orientation.

The first step in understanding non-spherical particle behaviour is to track the trajectory and orientation of single particles in a given flow field. Starting with the work of Jeffery (1922) on the behaviour of a single ellipsoid in viscous shear flows, analytical studies on isolated anisotropic particles in steady and unsteady laminar flows are available in the literature. In his formulation for the resistance force and torque on ellipsoids in uniform shear flow under Stokes conditions, Jeffery (1922) showed that the axis of symmetry of a spheroid performs a periodic motion on a closed orbit, the so-called "Jeffery" orbit. He concluded that the final state of a spheroid depends on its initial orientation, with the spheroid's motion being that which results in the minimum average dissipation of energy. Brenner, in a series of publications, e.g. (Brenner, 1963, 1964), expanded Jeffery's analysis to arbitrary flow fields, however, both Jeffery's and Brenner's works are in the absence of fluid and particle inertia. Many researchers have subsequently extended these works to study non-spherical particle suspensions in more general terms, including inertial effects and turbulent flow regimes. For example, Karnis et al. (1963, 1966) observed that at large Reynolds number, inertial effects become significant, making the non-spherical particles exhibit behaviour different from Jeffery's theory. They reported that neutrally buoyant particles in a Newtonian fluid move towards the region of maximum energy dissipation, although with insignificant change in the particle rotation.

Following growing interest in the subject, physical modelling and different numerical modelling approaches have been used to study the motion of non-spherical particles in various flow fields, with an extensive literature having been produced. Carlsson et al. (2006) used a charge-coupled device to analyse the velocity and orientation of fibres suspended in a shear flow moving over a solid wall. Holm and Söderberg (2007) applied an index-of-refraction matching method, together with particle tracking techniques, to study the influence of the near-wall shear stress on fibre orientation with different fibre aspect ratios and concentrations. Dearing et al. (2012) applied and validated a comprehensive methodology based on simultaneous single camera, two-phase PIV measurements to obtain fibre orientation and distribution, as well as flow field data, in a turbulent pipe flow. Hakansson et al. (2013) observed fibre streaks using a camera, and measured flow velocity profiles using laser Doppler velocimetry, in their experiments which used fibre suspensions in a turbulent half-channel flow. All these works have demonstrated that fibres accumulate in the near-wall region, preferentially concentrating in regions of low-speed velocity streaks, and tend to align with the mean flow direction.

Direct numerical simulation (DNS), in particular, has been used to study many aspects of these flows. Feng et al. (1994), for example, used DNS to investigate the motion of neutrally and non-neutrally buoyant circular particles in plane Couette and Poiseuille flows, with qualitative agreement recorded against results obtained from experimental measurement and perturbation theories. Others have studied the statistics, dispersion and deposition of ellipsoidal particles in turbulent channel flow using DNS. A wide range of classes of prolate spheroids have been considered using this approach, with the particles characterised by their different elongation (quantified by the particle aspect ratio, λ) and inertia (quantified by a suitably defined particle response time, τ_p^+), and transported in flows with different levels of turbulence (quantified by the shear Reynolds number, Re_τ) (Zhang et al., 2001; Mortensen et al., 2008a; Marchioli et al., 2010). Here, the particle response (or relaxation) time, τ_p , is the

response of the particle to the perturbations produced by the underlying turbulence, and the flow Reynolds number. The particle Stokes number, St , is then ratio of the particle response time, τ_p , to a characteristic time of the flow, τ_f . When the particle relaxation time is made dimensionless using wall variables, the resulting particle Stokes number is given by $St = \tau_p^+ = \tau_p/\tau_f$, where $\tau_f = \nu/u_\tau^2$, ν is the fluid kinematic viscosity and u_τ is the shear velocity. The shear Reynolds number $Re_\tau = hu_\tau/\nu$, with h the channel half-height. These authors (Zhang et al., 2001; Mortensen et al., 2008a; Marchioli et al., 2010) observed that, similar to spheres, prolate spheroids accumulate in the viscous sub-layer and preferentially concentrate in regions of low-speed fluid. They also tend to align with the mean flow direction, particularly very near the wall where their lateral tilting is suppressed. Tian et al. (2012) also used commercial CFD software to study low Reynolds number flows, reporting that the flow shear rate, the particle aspect ratio, different equivalent sphere sizes and the particle-to-fluid density ratio all significantly affect the transport and deposition of regular non-spherical particles. These authors also reviewed four frequently encountered equivalent sphere prescriptions used in the literature. Of the four, earlier work (Zhang et al., 2001; Mortensen et al., 2008a; Marchioli et al., 2010) only applied the equivalent Stokes sphere developed by Shapiro and Goldenberg (1993), and did not consider platelet-like particles ($\lambda < 1$). They also adopted Jeffery and Brenner's model for the general hydrodynamic forces and torques acting on an ellipsoidal particle in an arbitrary flow field. The Jeffery method is, however, limited to ellipsoidal particles with particle Reynolds numbers $Re_p \sim O(1)$, where $Re_p = |\mathbf{u}_f - \mathbf{v}|d_{ev}/\nu$ (for volume equivalent diameter, d_{ev} , and particle slip velocity ($\mathbf{u}_f - \mathbf{v}$)), and there remains continued interest in the dynamics of finite Reynolds number particles beyond the Stokesian regime. In addition, the dynamics of even the simplest non-spherical particles is often not well understood.

The lattice Boltzmann method has also been applied to study the effect of inertia and initial orientation on the dynamics of ellipsoidal particles suspended in shear flow (Ding and Aidun, 2000) and in Couette flow (Qi and Luo, 2002, 2003), with different states found depending on the Reynolds number range and the particle shape. Here, the shear Reynolds number is defined as (Huang et al., 2012) $Re_\tau = 4Gd^2/\nu$, where $G = 2U/N_y$ is the shear rate, d is the length of the semi-major axis of the particles, U is the velocity of the moving wall and N_y is the number of nodes along the velocity gradient direction. Qi and Luo (2002, 2003) identified the following modes for $Re_\tau < 467$: tumbling, precessing and nutating, log rolling and inclined rolling for a prolate spheroid; and for an oblate spheroid, log rolling and inclined rolling as Reynolds number increases. Huang et al. (2012) considered $0 < Re_\tau < 700$, beyond the range studied by Qi and Luo (2002, 2003), and reported seven rotational transitions and eight steady or periodic modes, with the modes identified by Qi and Luo (2002, 2003) a subset of these. Glowinski et al. (1999) and Glowinski et al. (2001) introduced the distributed Lagrange multiplier/fictitious-domain (DLM/FD) method for the numerical simulation of neutrally buoyant particles in a two-dimensional Poiseuille flow, later extending (Pan et al., 2008) the method to non-spherical particles and performing DNS of the motion of neutrally buoyant ellipsoids in a three-dimensional Poiseuille flow. In this work they investigated the orientational and rotational behaviour of an ellipsoid at Reynolds numbers up to 80, and found its rotation exhibits distinctive states depending on the Reynolds number range and particle shape. Yu et al. (2007) also studied the rotation of a single spheroid in a planar Couette flow at moderate Reynolds number, with $Re_\tau < 256$, using the DLM/FD method, identifying an extra mode for the oblate spheroid, i.e. the motionless mode, in addition to those noted by Qi and Luo (2003), and finding that the orbital behaviour of the prolate spheroid is sensitive to its initial orientation.

Other methods which take into account particle shape and the forces acting on non-spherical particles over a wide range of particle Reynolds number have been developed, e.g. (Yin et al., 2003, 2004; Mandø and Rosendahl, 2010). Yin et al. (2003, 2004) modelled particle motion in a non-uniform flow in order to better understand the combustion of non-spherical particles, where both their translational and rotational dynamics in the absence of fluid rotation were studied. In (Yin et al., 2003), the authors tracked cylindrical PVC particles in undisturbed stagnant water that became a non-uniform flow field under the influence of large settling particles. In (Yin et al., 2004), the authors employed cylinders and disks, rather than spheres, as an improved geometrical approximation to the shape of biomass such as straw and wood chips, implementing their method within a Reynolds-averaged Navier-Stokes modelling approach. The authors suggested using available drag correlations depending on shape, and accounting for the dependence of orientation by using the projected area. The particle rotational motion was investigated on the assumption of two dominating torques: that introduced by hydrodynamic forces due to the non-coincident centres of mass and pressure which determines the particle's orientation with respect to its direction of motion in the flow field, and the torque due to the resistance on a relatively rotating body, which always acts to attenuate the relative rotation. The torque due to the resistance as applied originally (Yin et al., 2003) did not consider fluid rotation, making the model more suitable for the sedimentation of non-spherical particles in a stagnant fluid. The later application (Yin et al., 2004) used their force and torque models to simulate co-firing biomass with methane, with comparisons with data on the motion of a cylindrical particle in a non-uniform flow field showing good agreement for both the particle translational and rotational dynamics. The Yin et al. (2003, 2004) model has also been successfully applied by Zastawny et al. (2012) to develop drag and lift coefficients, and by Njobuenwu and Fairweather (2013a, 2014) to model the effect of shape on particle behaviour. Njobuenwu and Fairweather (2013b, 2014) modified the Yin et al. (2003) model to account for ellipsoidal particles (oblate and prolate spheroids), initially neglecting fluid rotation (Njobuenwu and Fairweather, 2014) when computing the torque due to resistance to relative rotation, but accounting for it in (Njobuenwu and Fairweather, 2013b). Both research groups (Zastawny et al., 2012; Njobuenwu and Fairweather, 2014) again show that shape has a large influence on the behaviour of a particle, particularly in terms of the forces and torques the particle experiences.

The aim of the present work was to study the effect of particle shape, inertia, initial orientation and position within the boundary layer in a turbulent channel flow on the translational and orientational behaviour of single non-spherical particles, assuming one-way coupling between the fluid and the particles. Most of the reported research efforts in this area, i.e. on single particle dynamics, have focused on analytical solutions in frozen flow fields, and in many cases, only prolate spheroids have been considered. However, the characteristic translational and rotational dynamics of non-spherical particles resulting from their interactions with the turbulent environment has not been fully elucidated. This study considers a number of particle aspect ratios, with $\lambda < 1$ for oblate spheroids, $\lambda = 1$ for spheres, and $\lambda > 1$ for prolate spheroidal particles, which complements other studies available in the literatures. Another important aspect of the present work is that the particle size is based on the equivalent volume diameter, where particles with the same relaxation time have equal mass, volume and density. Hence, any difference in the behaviour amongst particles with the same relaxation time will be as a result of the difference in shape and orientation alone. The fluid phase is described as a continuum in an Eulerian framework, with the time-dependent flow and turbulence predicted using large eddy simulation, with the sub-grid scale motions modelled

using a dynamic approach. The motion of non-spherical particles is computed in a Lagrangian framework using a point-wise approximation (which means that for the largest needle-like particles results are likely to be qualitatively rather than quantitatively accurate). The particle's non-sphericity is modelled by coupling Lagrangian particle tracking with the Euler equation of rotational motion in the particle frame. The study is based on the approach of Yin et al. (2003) and extends earlier work (Njobuenwu and Fairweather, 2013a, 2013b, 2014) by accounting for fluid rotation in a dynamic system when computing the torque due to the resistance to relative rotation of a rigid non-spherical particle.

2. Numerical simulations

2.1. Large eddy simulation

With the rapid advancements in, and successes reported for, large eddy simulation (LES) of multiphase flows in various geometries, the LES technique is employed for the fluid phase in an Eulerian framework. LES resolves the large-scale energetic motions and models the sub-grid scale (SGS) motions. The top-hat filtered governing equations of motion for an incompressible fluid are given for mass and momentum, respectively, as:

$$\frac{\partial \bar{u}_j}{\partial x_j} = 0, \quad (1)$$

$$\frac{\partial \bar{u}_i}{\partial t} + \bar{u}_j \frac{\partial \bar{u}_i}{\partial x_j} = -\frac{1}{\rho} \frac{\partial \bar{p}}{\partial x_i} - \frac{\partial}{\partial x_j} (\bar{\sigma}_{ij} + \tau_{ij}), \quad (2)$$

where $\bar{\sigma}_{ij} = -2\nu \bar{s}_{ij}$ represents the viscous stress, $\bar{s}_{ij} = \frac{1}{2}(\partial \bar{u}_i / \partial x_j + \partial \bar{u}_j / \partial x_i)$ is the filtered strain-rate tensor, ν is the kinematic viscosity, $\tau_{ij} = \bar{u}_i \bar{u}_j - \bar{u}_i \bar{u}_j$ represents the effect of the SGS motion on the resolved motion (known as the SGS stress), t is time, x_j is the spatial co-ordinate directions, u_j is the velocity vector, p is the pressure, and ρ is the density. The SGS stress term is computed using the dynamically calibrated version of the Smagorinsky model (Germano et al., 1991). This technique represents the SGS stresses as the product of a SGS viscosity, ν_{SGS} , and the resolved part of the strain tensor, with the SGS viscosity evaluated as the product of the filter width, Δ , and an appropriate velocity scale, $\Delta |\bar{s}|$. Hence, the anisotropic part of the SGS stresses is given by:

$$\tau_{ij}^a = -2(C\Delta)^2 |\bar{s}| |\bar{s}|^a \quad (3)$$

where the model coefficient C must be estimated, with this achieved by applying a second filtering operation, denoted by (\sim) to Eq. (2). In the test filtered equation the SGS stresses are:

$$T_{ij} = \bar{u}_i \bar{u}_j - \tilde{\bar{u}}_i \tilde{\bar{u}}_j. \quad (4)$$

Both T_{ij} and $\tilde{\bar{u}}_{ij}$ are unknown but are related by Germano's identity (Germano et al., 1991) through the resolved stress tensor:

$$L_{ij} = T_{ij} - \tilde{\bar{u}}_{ij} = \bar{u}_i \bar{u}_j - \tilde{\bar{u}}_i \tilde{\bar{u}}_j, \quad (5)$$

which can be computed from the resolved quantities. To give the required expression for C in Eq. (3), some form of relationship between the model constant values C and $C^2(\tilde{\bullet})$ at the grid- and test-filter levels must be specified and, based on the hypothesis that the cut-off length falls inside the inertial sub range, $C^2 = C^2(\tilde{\bullet})$. However, such a sub-range is not guaranteed to occur in wall bounded or low Reynolds number flows, with the largest deviation from universality of the SGS motions expected to occur in the regions of weakest resolved strain. Based on this, the two values of the model parameter at two different filter levels are likely to differ. To account for this, di Mare and Jones (2003) proposed the

following:

$$C^2(\bullet) = C^2 \left(1 + \frac{\varepsilon}{2\sqrt{2}\Delta^2 \|\tilde{s}\| \|\tilde{s}^a\|^2} \right) \quad (6)$$

where ε is assumed as the dissipation rate, such that $\varepsilon \approx v^3/l$; v and l are the velocity and length scales respectively, such that $v = u_b$ and $l = h$, where u_b and h are the bulk velocity and channel half-width.

Eq. (6) assumes that the scale invariance of C can only be invoked if the cut-off falls inside an inertial sub-range, and when this occurs, the modelled dissipation should represent the entire dissipation in the flow. Conversely, in the high Reynolds number limit, the dissipation is only determined by v and l so that the ratio of ε to $\Delta^2 \|\tilde{s}\|^3$ is a measure of how far the flow is from scale preserving conditions. This equation represents a first-order expansion of other scale dependent expressions for C , e.g. that of Port-Agel et al. (2000), which also use a single length and velocity scale. Eqs. (5) and (6), with contraction of both sides with the tensor \tilde{s} , then give

$$C^2 = \frac{[2\sqrt{2}(C_*^2\Delta)^2 \|\tilde{s}\| \|\tilde{s}^a\| - L_{ij}^a \tilde{s}_{ij}^a]}{\varepsilon + 2\sqrt{2}\Delta^2 \|\tilde{s}\| \|\tilde{s}^a\|^2} \quad (7)$$

where C_*^2 is a provisional value for the field C^2 , for example, its value at the previous time step (Piomelli and Liu, 1995). The dependence embodied in Eq. (6) gives a simple correlation for C^2 . The main advantage of the method is that it is well conditioned and avoids the spiky and irregular behaviour exhibited by some implementations of the dynamic model and, as the resolved strain tends to zero, C^2 also tends to zero, while $C^2(\bullet)$ remains bounded. Eq. (7) also yields smooth C^2 fields without a need for averaging, and the maxima of C^2 are of the same order of magnitude as Lilly (1967) estimate for the Smagorinsky model constant. However, Eq. (7) does not prevent negative values of the model parameter, with such values set to zero to prevent instability. Negative values of the SGS viscosity are similarly set to zero. In the present work, test filtering was performed in all space directions, with no averaging of the computed model parameter field. The ratio Δ^2/Δ was set to 2 and the filter width determined from $\Delta = (\Delta_x \Delta_y \Delta_z)^{1/3}$.

2.2. Particle equations of motion

Three reference frames are invoked to describe an ellipsoidal particle (spheroid), as shown in Fig. 1; $\mathbf{x} = [x, y, z]$ is referred to as the inertial or external frame, $\mathbf{x}' = [x', y', z']$ represents the particle frame while $\mathbf{x}'' = [x'', y'', z'']$ is called the co-moving frame. The origin of both the particle and co-moving frames is at the particle centroid, while the axes of the co-moving frame are parallel to the corresponding axes of the inertial frame.

The Euler angles (ϕ, θ, ψ) define the particle orientation, as shown in Fig. 1. The surface of a super-quadratic ellipsoidal particle in the particle reference frame is given as (Hilton and

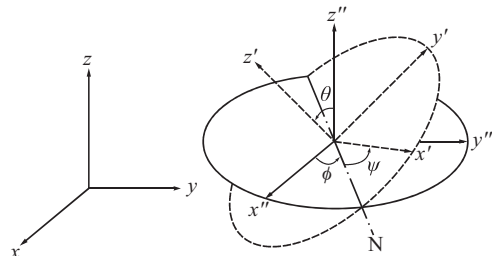


Fig. 1. Relationship between the inertial $\mathbf{x} = [x, y, z]$, the particle $\mathbf{x}' = [x', y', z']$ and the co-moving $\mathbf{x}'' = [x'', y'', z'']$ co-ordinate systems and definition of the Euler angles (ϕ, θ, ψ) . $N = \text{plane } [x', y'] \cap \text{plane } [x'', y'']$, θ is the angle between the z' -axis and z'' , ϕ is the angle between the x'' -axis and N , and ψ is the angle between the x' -axis and N .

Cleary, 2011)

$$\left(\frac{x'}{a} \right)^2 + \left(\frac{y'}{b} \right)^2 + \left(\frac{z'}{c} \right)^2 = 1 \quad (8)$$

where a, b and c represent the lengths of the three semi-principal axes of a spheroid in the x' -, y' - and z' -directions, respectively. Three special cases of super-ellipsoids are considered: spherical ($\lambda = 1$), oblate ($\lambda < 1$), and prolate ($\lambda > 1$) spheroids, where $\lambda = c/a$ is the aspect ratio of the spheroid, and $a=b$ in all cases. The transformation between the co-moving frame and the particle co-ordinates is expressed as

$$\mathbf{x}' = \mathbf{A} \cdot \mathbf{x}'' \quad (9)$$

The transformation matrix $\mathbf{A} = [a_{ij}]$ can be expressed with respect to either Euler angles, (ϕ, θ, ψ) or Euler parameters (or quaternions), $\mathbf{q} = [q_0, q_1, q_2, q_3]$ (Goldstein, 1980). Previous investigations (Fan and Ahmadi, 1995; Yin et al., 2003) have shown that the use of Euler angles is very inefficient because of the singularity problem whenever the Euler angle is 0 or π . The use of four Euler quaternions overcomes this problem (Fan and Ahmadi, 1995). Hence, the particle rotational dynamics is therefore determined in terms of the quaternions. The orientational matrix \mathbf{A} in terms of the quaternion \mathbf{q} is given by:

$$\mathbf{A} = \begin{bmatrix} 1 - 2(q_2^2 + q_3^2) & 2(q_1 q_2 + q_0 q_3) & 2(q_1 q_3 - q_0 q_2) \\ 2(q_1 q_2 - q_0 q_3) & 1 - 2(q_1^2 + q_3^2) & 2(q_2 q_3 + q_0 q_1) \\ 2(q_1 q_3 + q_0 q_2) & 2(q_2 q_3 - q_0 q_1) & 1 - 2(q_1^2 + q_2^2) \end{bmatrix} \quad (10)$$

where the individual quaternions are obtained from the Euler angles as:

$$\begin{aligned} q_0 &= \cos \frac{\phi+\psi}{2} \cos \frac{\theta}{2} & q_1 &= \cos \frac{\phi-\psi}{2} \sin \frac{\theta}{2} \\ q_2 &= \sin \frac{\phi-\psi}{2} \sin \frac{\theta}{2} & q_3 &= \sin \frac{\phi+\psi}{2} \cos \frac{\theta}{2} \end{aligned} \quad (11)$$

The quaternions are subject to the constraint

$$q_0^2 + q_1^2 + q_2^2 + q_3^2 = 1 \quad (12)$$

2.2.1. Translational motion

A force \mathbf{F} applied on a non-spherical particle away from its centroid simultaneously changes two properties of the particle: the linear motion of the centroid and the angular motion around the centroid. The former is governed by Newton's equation of motion:

$$m_p \frac{d\mathbf{v}}{dt} = \mathbf{F}_D + \mathbf{F}_L \quad (13)$$

$$\frac{d\mathbf{x}_p}{dt} = \mathbf{v} \quad (14)$$

where $\mathbf{x}_p = [x_p, y_p, z_p]$ and $\mathbf{v} = [v_x, v_y, v_z]$ represent the particle position and velocity vector, $m_p = 4\pi a^3 \lambda \rho_p / 3$ is the mass of the particle, and \mathbf{F}_D and \mathbf{F}_L represent drag and profile lift forces acting on the particle. Note that the unsteady particle-fluid hydrodynamic forces (e.g. Basset, pressure gradient, added mass) are not accounted for since their effects are negligible for gas-solid flows with $\rho/\rho_p \ll 1$ (Broday et al., 1998; Njobuenwu et al., 2013). The shear (Saffman) lift force is important, especially in the near-wall region, but is generally smaller than the drag force, even in this region. In this work its effect was neglected for the sake of improving understanding of fluid-particle interaction within a manageable parameter range. This is common practice in the DNS and LES of particle-laden, two-phase flow in a channel (Wang and Squires, 1996a, 1996b; Marchioli et al., 2008, 2010; Mortensen et al., 2008a, 2008b; Zhao et al., 2012). For small sizes of ellipsoidal particles, the drag force also exhibits a greater influence on the particle dynamics than the lift force (Wang et al., 1997; Pan et al., 2001). In addition, since the particle shapes are

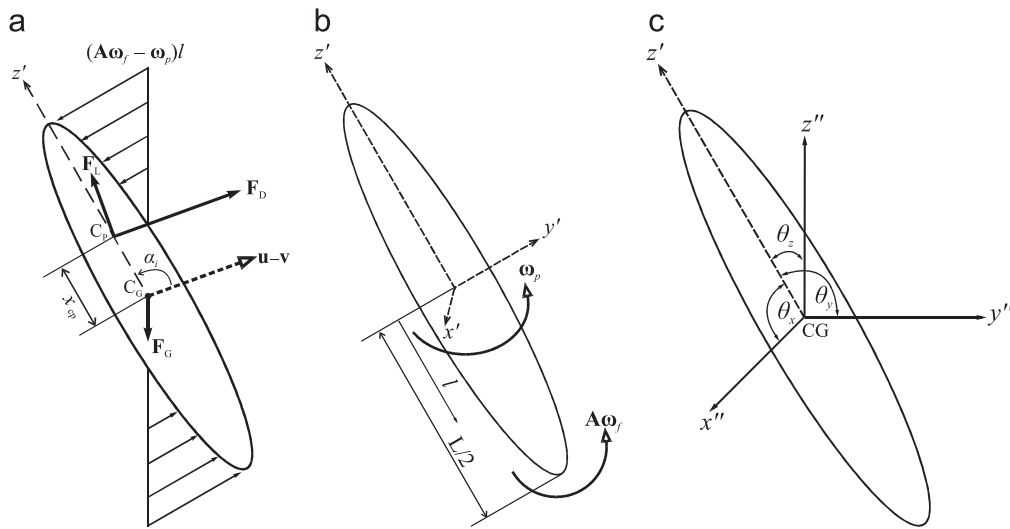


Fig. 2. (a, b) Illustration of torque due to resistance on a rotating particle and the location of the centres of gravity (CG) and pressure (CP), the incident angle α_i and the forces acting on the particle (x_{cp} is the distance between CG and CP, and the incidence angle α_i is the angle between the slip velocity $|\mathbf{u} - \mathbf{v}|$ and the particle major axis z'); (c) Definition of angles θ_x , θ_y and θ_z which are, respectively, the angle between the particle principal axis z' and its co-moving axes x'' , y'' and z'' .

subjected to the same force balance and turbulence intensity, it may be assumed that the conclusions reached from the analysis performed will be correct. A high particle relaxation time implies that the body forces (e.g. gravity) are normally important in the analysis of particle motion (Marchioli and Soldati, 2007), however, in this work gravity is not accounted for in order to focus on the effects of particle inertia, shape, orientation and interaction with the fluid. Neglecting gravity in a particle-laden two phase flow simulation has been employed previously for similar reasons by a number of authors, e.g. (Marchioli and Soldati, 2007; Marchioli et al., 2008, 2010). The drag and profile lift forces resulting from particle orientation are given, according to (Yin et al., 2003), as:

$$\mathbf{F}_D = \frac{1}{2} \rho A_D C_D |\mathbf{u}_f - \mathbf{v}| (\mathbf{u}_f - \mathbf{v}), \quad (15)$$

$$\mathbf{F}_L = \frac{1}{2} \rho A_L C_L \frac{\mathbf{z}' \cdot (\mathbf{u}_f - \mathbf{v})}{|\mathbf{u}_f - \mathbf{v}|} [\mathbf{z}' \times (\mathbf{u}_f - \mathbf{v})] \times (\mathbf{u}_f - \mathbf{v}), \quad (16)$$

where $\mathbf{u}_f = [u_x, u_y, u_z]$ is the fluid velocity vector at the particle centroid, \mathbf{z}' is the direction of the particle major axis in the inertial frame, which means that it is transformed from the particle to the inertial frame using Eq. (9), and A_D and A_L are the particle projected areas normal to the direction of the drag and lift forces, respectively. The projected areas A_D and A_L expressed as a function of the incidence angle provide coupling between translational and rotational motion. The areas A_D and A_L can be expressed as a function of the particle incidence angle, α_i , between the particle slip velocity, $(\mathbf{u}_f - \mathbf{v})$, and the particle principal axis, z' , see Fig. 2, as (Yin et al., 2003):

$$A_D = \pi a^2 \left[\cos^2 \alpha_i + (4\lambda/\pi)^2 \sin^2 \alpha_i \right]^{1/2} \quad (17)$$

$$A_L = \pi a^2 \left[\sin^2 \alpha_i + (4\lambda/\pi)^2 \cos^2 \alpha_i \right]^{1/2} \quad (18)$$

where $A_D = \pi a^2$ for a spherical particle with $\lambda = 1$. The drag coefficient, C_D , in Eq. (15) is obtained from correlations for non-spherical particles available in the literature. Note that the incidence angle is required to determine the forces and torques.

Several authors have proposed drag correlations that apply to particles of several different shapes. Chhabra et al. (1999) compared five available drag coefficient correlations for non-spherical particles (Haider and Levenspiel, 1989; Swamee and Ojha, 1991; Ganser, 1993; Chien, 1994; Hartman et al., 1994) by using 1900 data points

covering a wide range of physical and kinematic conditions such as particle Reynolds number $10^{-4} < Re_p < 5 \times 10^5$, particle sphericity $0.09 < \Phi < 1.0$, and particle shape (cylinders, needles, cones, prisms, discs, cubes) from 19 independent studies. Note that the particle sphericity, Φ , is defined as the ratio of the surface area of a sphere having the same volume as the particle to the actual surface area of the non-spherical particle. They compared the overall mean and maximum percentage errors using the same set of data for the five correlations and found that the Ganser (1993) correlation was the most accurate with an average error of 16.3%. Ganser's correlation is based on the fact that every particle experiences a Stokes regime where drag is linearly related to the velocity, and a Newton regime where drag is proportional to the square of the velocity, and introduces two shape factors, K_1 and K_2 , applicable in the Stokes and Newton flow regimes, respectively. Ganser's method is adopted here with the correlation given as:

$$\frac{C_D}{K_2} = \frac{24}{Re_p K_1 K_2} \left[1 + 0.118 (Re_p K_1 K_2)^{0.6567} \right] + \frac{0.4305}{1 + 3305/(Re_p K_1 K_2)} \quad (19)$$

where $Re_p = |\mathbf{u}_f - \mathbf{v}| d_{ev} / \nu$ is the particle Reynolds number based on the volume equivalent diameter, d_{ev} , the particle slip velocity $(\mathbf{u}_f - \mathbf{v})$ and the fluid kinematic viscosity ν , $K_1 = (\frac{1}{3} d_n / d_{ev} + \frac{2}{3} \Phi^{-0.5})$ and $K_2 = 10^{1.8148(-\log \Phi)^{0.543}}$ are unique coefficients that model the sphericity of a spherical particle, or the particle sphericity and orientation for non-spherical particles. The volume equivalent diameter $d_{ev} = 2a\lambda^{1/3}$ is the diameter of a sphere having the same volume as the non-spherical particle, while the projected area diameter $d_n = (4A_D/\pi)^{1/2}$ is the diameter of a circle having the same area as the projection of the non-spherical particle. To emphasise the coupling between the Newton and Euler equations, the particle orientation is accounted for in the drag force in Eq. (15) by A_D , the particle projected area normal to the direction of the drag, and by the drag coefficient C_D . The projected area on which the drag is based, given in Eq. (17), is expressed as a functional relationship of the incidence angle α_i and the particle's dimensions a , c . Using an analogy from the aerodynamic theory of wing sections it is possible to define the incidence angle as the angle between the principal axis z' and the direction of motion, represented as the particle slip velocity, as shown in Fig. 2. At every time step (or iteration), a new α_i is based on the instantaneous particle orientation. Mathematically, the new α_i is obtained from the transformation of $(\mathbf{u}_f - \mathbf{v})$ with the

third row of the elements of the orientational matrix \mathbf{A} of Eq. (9). The projected area may be several orders of magnitude different from one orientation to another. The drag coefficient also varies significantly depending on the orientation. In C_D , Eq. (19), the dynamic equal-projected area circle diameter, d_n , is a function of A_D and has to be updated for every incidence angle. The lift coefficient C_L in Eq. (16) is determined such that the ratio of lift to drag forces satisfies the relationship (Yin et al., 2003):

$$\frac{|C_L|}{|C_D|} = \left| \sin^2 \alpha_i \cos^2 \alpha_i \right| \quad (20)$$

Following (Besnard and Harlow, 1986), the profile lift has limiting cases such that for a spherical particle ($\lambda = 1$) there is no rotation nor lift of the particle, hence only drag is applied. Likewise, for an infinitely massive particle, there is no motion; if $\alpha_i = \pi/2$, there is no torque; and for $\alpha_i = 0$, there is no profile lift. Note, a common approach used in the literature is to assume that the profile lift is proportional to the drag, and that the dependence with the orientation is given by the so-called 'cross-flow principle' (Mandø and Rosendahl, 2010). Based on this, the approach of Yin et al. (2003) has been adopted, with the limitations of this approach discussed in detail elsewhere (Mandø and Rosendahl, 2010; Njobuenwu and Fairweather, 2014).

2.2.2. Rotational motion

The rate of change with time of the principal components of the angular velocity $\boldsymbol{\omega} = (\omega_x, \omega_y, \omega_z)$ is given by Euler's equation as:

$$\mathbf{I} \frac{d\boldsymbol{\omega}}{dt} = \mathbf{T}_{\text{offset}} + \mathbf{T}_{\text{resist}} + \mathbf{T}_{\text{crossterm}} \quad (21)$$

where \mathbf{I} is the moment of inertia tensor, and $\boldsymbol{\omega}$ is the angular velocity vector. The principal moments of inertia of a spheroid are $I_x = I_y = \frac{1}{5} m_p a^2 (1 + \lambda^2)$ and $I_z = \frac{2}{5} m_p a^2$. $\mathbf{T}_{\text{offset}}$ is the torque due to non-coincidence of the centres of gravity and pressure, and takes account of the hydrodynamic force effect as illustrated in Fig. 2. The aerodynamic forces act at CP which is located a distance x_{cp} from CG. Using the particle major axis, \mathbf{z}' , and the transformation matrix, \mathbf{A} , $\mathbf{T}_{\text{offset}}$ is given in the particle frame of reference as (Yin et al., 2003)

$$\mathbf{T}_{\text{offset}} = \mathbf{A}[(x_{\text{cp}} \mathbf{z}') \times (\mathbf{F}_D + \mathbf{F}_L)] \quad (22)$$

where $\mathbf{T}_{\text{offset}}$ will change its sign, such that $\mathbf{T}_{\text{offset}} = -\mathbf{T}_{\text{offset}}$ when $\cos \alpha_i > 0$, and

$$x_{\text{cp}} = 0.25 a_z (1 - e^{3(1-\lambda)}) |\cos^3 \alpha_i|, \quad (23)$$

which is based on a semi-empirical expression proposed in (Yin et al., 2003). $\mathbf{T}_{\text{resist}}$ in Eq. (21) is the torque due to resistance to rotation, which always acts to attenuate the angular velocity and can be directly derived by integration of the friction, caused by rotation, over the particle length, L . $\mathbf{T}_{\text{resist}}$ for spheroidal particles under Stokes flow conditions is known (Jeffery, 1922) and has also been expanded to other shapes (Cox, 1971) and to higher Reynolds numbers (Mandø and Rosendahl, 2010). The local relative spin of the fluid due to particle rotation is $(\mathbf{A}\boldsymbol{\omega}_f - \boldsymbol{\omega}_p)$, where $\boldsymbol{\omega}_f = \frac{1}{2} \nabla \times \mathbf{u}$ accounts for the fluid undisturbed vorticity at the point occupied by the particle's centre of mass, with respect to the particle frame, which has been related to the local velocity gradient (Yin et al., 2003, 2004); l is the distance from the centre of rotation (see Fig. 2). The resulting torque is thus expressed as:

$$\mathbf{T}_{\text{resist}} = \pm \int_0^{L/2} C_D \rho_f A_D [(\mathbf{A}\boldsymbol{\omega}_f - \boldsymbol{\omega}_p) l]^2 dl \quad (24)$$

where the sign (\pm) of $\mathbf{T}_{\text{resist}}$ is selected as the sign of $(\mathbf{A}\boldsymbol{\omega}_f - \boldsymbol{\omega}_p)$, as illustrated in Fig. 2. $\mathbf{T}_{\text{crossterm}} = [T_x', T_y', T_z']$ in Eq. (21) with respect to the particle axes $\mathbf{x}' = [x', y', z']$ is given by:

$$T_x' = \omega_y \omega_z (I_y - I_z) \quad (25)$$

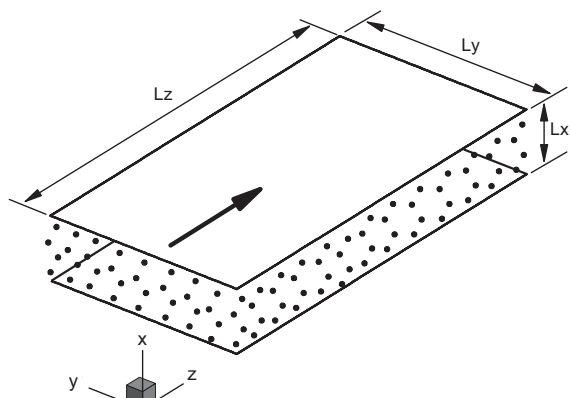


Fig. 3. Schematic of the computational domain of the channel flow.

$$T_y' = \omega_z \omega_x (I_z - I_x) \quad (25)$$

$$T_z' = \omega_x \omega_y (I_x - I_y) \quad (25)$$

The time evolution of the quaternion is used to update the orientation of the particles and is computed from:

$$\dot{\mathbf{Q}} = \begin{pmatrix} \dot{q}_0 \\ \dot{q}_1 \\ \dot{q}_2 \\ \dot{q}_3 \end{pmatrix} = \frac{1}{2} \begin{bmatrix} q_0 & -q_1 & -q_2 & -q_3 \\ q_1 & q_0 & -q_3 & q_2 \\ q_2 & q_3 & q_0 & -q_1 \\ q_3 & -q_2 & q_1 & q_0 \end{bmatrix} \begin{bmatrix} 0 \\ \omega_x \\ \omega_y \\ \omega_z \end{bmatrix} \quad (26)$$

Lastly, it should be noted that there is coupling between the translational and rotational motion. In Eq.(22), the torque due to the non-coincident centres of mass and of pressure, $\mathbf{T}_{\text{offset}}$, is a function of the hydrodynamic force in the inertial frame which is transformed to the particle frame by the transformation matrix \mathbf{A} . For each time or integration step, the transformation matrix is obtained from the new quaternions, and these quaternions are subsequently used to obtain new values of α_i , A_D , d_n , C_D , F_D and $\mathbf{T}_{\text{offset}}$. This is also the case for the torque due to the resistance on a relatively rotating body, $\mathbf{T}_{\text{resist}}$, which is a function of A_D and C_D .

3. Numerical solution

The channel flow employed had the configuration: inertial coordinates ($x \times y \times z$), computational domain size ($2h \times 2\pi h \times 4\pi h$) and grid nodes ($129 \times 128 \times 128$) in the wall-normal, spanwise and streamwise directions, respectively, as shown in Fig. 3. The shear Reynolds number $Re_\tau (= hu_\tau/\nu)$ was 300 based on the shear velocity $u_\tau = 0.2355 \text{ ms}^{-1}$ and the bulk Reynolds number $Re_b (= hu_b/\nu)$ was 4910 based on the bulk velocity $u_b \sim 3.855 \text{ m s}^{-1}$, respectively, with the channel half-height $h = 0.02 \text{ m}$, kinematic viscosity $\nu = 1.57 \times 10^{-5} \text{ m}^2 \text{ s}^{-1}$ and density $\rho = 1.3 \text{ kg m}^{-3}$. The mesh spacing was uniform in the homogeneous (y - and z -) directions, but stretched in the inhomogeneous (x -) direction by a hyperbolic stretching function. The non-dimensional values of parameters associated with length, velocity and time are presented in wall units (+) following normalisation with u_τ and ν .

Periodic boundary conditions were applied in the homogeneous directions for both the fluid and particle phases. A mean pressure gradient was applied in the streamwise direction to maintain the mass flow rate. No-slip boundary conditions were applied at the walls for the fluid. The particle wall boundary condition is straightforward for spherical and non-trivial for ellipsoidal particles. In the absence of a detailed particle-wall interaction model for ellipsoidal particles, the model employed for spherical particles was used. This approach has been previously applied by a number of authors

(Zhang et al., 2001; Mortensen et al., 2008a; Marchioli et al., 2010; Zhao et al., 2014), with particles reflected elastically when the particle centre is half the equivalent sphere diameter from the wall. In such cases, the particle linear momentum in the wall-normal direction is changed in sign whereas the linear momentum in the two homogenous directions and the angular momentum are unchanged. To avoid laminarisation of the flow, an initial simulation at high Reynolds number ($Re_\tau \geq 300$) was carried out and the resulting solution was used to initialise the flow at $Re_\tau = 300$. The two-phase flow simulation started from the fully developed turbulent single phase flow. The particles' initial position and orientation were random, with the initial linear and rotational velocity vectors set equal to those of the fluid at the particle position.

The governing equations for the fluid phase were solved numerically using the finite-volume code BOFFIN (Boundary Fitted Flow Integrator) (Jones et al., 2002). The code is based on a fully implicit low-Mach number formulation and is second-order accurate in both space and time. The governing filtered equations in Cartesian co-ordinates can be transformed into a curvilinear co-ordinate system, although the equation set was solved in Cartesian co-ordinates in the present work, and the finite-volume approach is used to discretise the partial differential equations to yield a system of quasi-linear algebraic equations. To discretise the spatial derivatives in Eqs. (1) and (2), the standard second-order accurate central difference scheme is used, except for the convective terms in the momentum equation, Eq. (2), for which an energy conserving discretisation scheme is employed. The time derivatives in Eqs. (1) and (2) are approximated by a three point backward difference scheme with a variable time-step to ensure that the maximum Courant number, based on the filtered velocity, always lies between 0.1 and 0.2. The pressure is determined by a two-step, second-order, time-accurate approximate factorisation method. A co-located pressure and velocity arrangement is used and an odd/even node uncoupling of the pressure and velocity fields is prevented by a pressure smoothing technique (Rhee and Chow, 1983). The system of algebraic equations resulting from the discretisation is solved using the matrix pre-conditioned conjugate gradient methods BI-CGSTAB (van der Vorst, 1992) for the matrix of velocity vectors, and ICCG (Kershaw, 1978) for the pressure. The BOFFIN code has been applied extensively in the LES of reacting and non-reacting turbulent flows, e.g. (Bini and Jones, 2008; Njobuenwu and Fairweather, 2014). For further details of the numerical method used in BOFFIN, readers are referred to those publications and relevant references therein.

The particle equations of motion were integrated using an efficient fourth-order Runge–Kutta scheme. The computational procedure for the solution of the particle equations is similar to that described in (Yin et al., 2003). To avoid build-up errors, the quaternions are renormalized at every time-step using Eq. (12). The particle integration time for the translational and rotational motion is equal to the LES time step and smaller than the smallest particle response time. One-way coupling is assumed between the fluid and the particles. Considering the negligible volume fraction of a single particle suspended in the carrier phase, the adoption of one-way coupling is justified. During each time step, the fluid flow field is first updated and then interpolated to the particle position using a trilinear interpolation scheme, and then passed to the Lagrangian particle tracker. It is worthy of note that predictions obtained for particle dispersion in a turbulent channel flow using this interpolation scheme have been demonstrated (Marchioli et al., 2008) to yield results in line with those derived on the basis of higher order schemes.

Only values from the resolved velocity field were used to calculate the unsteady forces, thus neglecting the effect of the unresolved velocities on particle trajectories. At low Reynolds numbers, Armenio et al. (1999) reported that the unresolved velocity field was found to have a limited effect on the statistics of inertial particles. Wang and Squires (1996b) applied LES to study particle-laden channel flows at

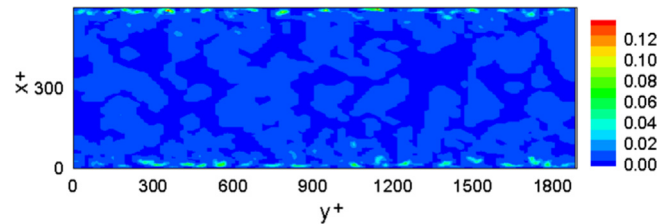


Fig. 4. Instantaneous sub-grid scale turbulence kinetic energy ($k_{sgs}/m^2 s^{-2}$) in the spanwise direction along a plane at $z=2\pi h$.

$Re_\tau = 180$ and 644 using $64 \times 65 \times 64$ grid points to discretise the filtered equations. These authors used a dynamic eddy viscosity model and added the SGS fluctuations to the particle velocity, demonstrating that these fluctuations contributed less than 1% of the total particle root-mean-square (rms) velocity fluctuations. In this study, significantly more grid nodes were used ($129 \times 128 \times 128$), effectively doubling the number of nodes in each co-ordinate direction. The instantaneous SGS kinetic energy obtained using the latter grid node distribution is given in Fig. 4. The SGS kinetic energy, k_{sgs} , shows how much energy is in the unresolved scales, as well as the likely contribution this energy makes to the particle dispersion. Values of $k_{sgs} \sim 0.13 m^2 s^{-2}$ was observed compared, for example, to $k_{sgs} \sim 1.9 m^2 s^{-2}$ obtained by Winkler (2002) when using a $64 \times 65 \times 32$ mesh. Further consideration of the effect of SGS velocity fluctuations on the motion of particles in the LES of particle-laden turbulent flow can be found elsewhere (Bini and Jones, 2007; Salmanzadeh et al., 2010). Overall, the influence of such fluctuations on the motion of particles depends on the flow Reynolds number and particle inertia, the numerical resolution used, and the filter function and precise SGS model employed. In this work, the parameters and variables adopted were such that the errors arising from neglecting the influence of the SGS velocity were kept to a minimum. These include the consideration of a low Reynolds number flow and inertial particles (Stokes number based on equivalent sphere diameter, $\tau_{eq}^+ \approx 1$), the use of top-hat filtering of the descriptive equations and a dynamic SGS model, as well as the use of a high nodal density to ensure a close to DNS resolution, particularly near the walls.

4. Results and discussion

4.1. Fluid phase validation

The relevant features of the flow field at those locations where the particle dynamics are reported and analysed are first presented. The instantaneous streamwise fluid velocity fluctuation (w') in wall units is shown in Fig. 5 on wall-parallel planes ($y-z$) in the buffer region ($x^+ \sim 8.0$) and at the channel centre ($x^+ = 300$). The instantaneous spanwise fluid vorticity $\omega_y = 0.5 \times (\partial w/\partial x + \partial u/\partial z)$ in wall units is shown in Fig. 6 on a plane ($x-z$) down the centre of the channel. The LES is seen to produce instantaneous turbulent structures resembling streaks in the layer at a distance of $x^+ \sim 8.0$ from the lower wall and at the channel centre, as shown in Fig. 5. From this figure, it is clear that the fluid velocity in the buffer region is generally less than the mean velocity of the entire channel, whilst at the centre, the velocity is evenly distributed about that mean. In addition, coherent structures in the spanwise vorticity are captured on the $x-z$ plane down the centre of the channel, as shown in Fig. 6. The unsteadiness in the flow can clearly be inferred from the small-scale structures visible in these plots. These well-known characteristics of a channel flow are well captured by the LES using the nodal distribution employed. The LES results are further

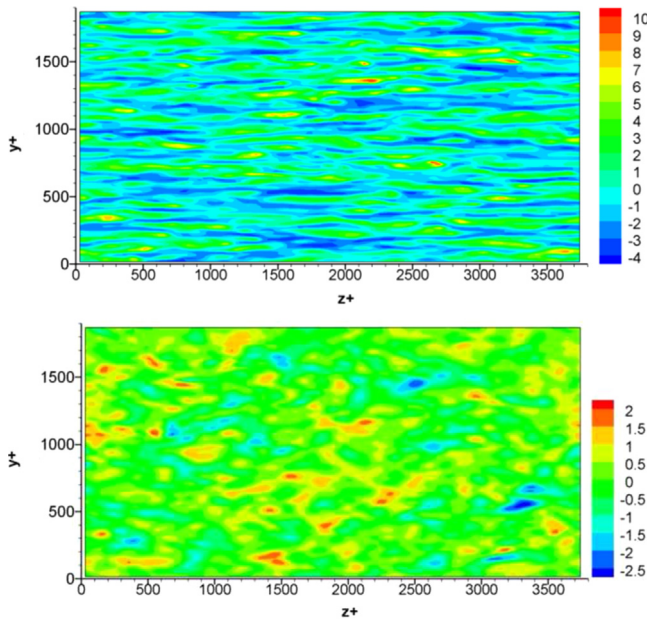


Fig. 5. Instantaneous streamwise fluid velocity fluctuation (w') in the streamwise direction along planes at $x^+ = 8$ (top) and $x^+ = 300$ (bottom).

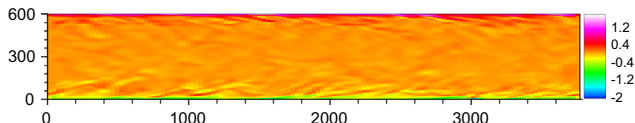


Fig. 6. Instantaneous spanwise vorticity (ω_y') in the streamwise direction along a plane at $y = \pi h$.

compared with DNS predictions (Marchioli and Soldati, 2007) for the single-phase flow in Fig. 7 for the streamwise mean velocity w^+ , the rms of the velocity fluctuations ($u'_{\text{rms}} +$, $v'_{\text{rms}} +$ and $w'_{\text{rms}} +$) in the wall-normal, spanwise and streamwise directions, and for the turbulent shear stress ($u' w' +$). There is in general good agreement between the LES and DNS results. The peak in the rms of the streamwise velocity fluctuation is slightly over-predicted, while the wall-normal and spanwise components are slightly under-predicted. The LES also generally under-predicts the velocity fluctuation profiles in all three directions towards the channel centre. Overall, however, the accuracy of these predictions demonstrates that the current LES is in sufficiently close agreement with the DNS to warrant its use in analysing the dynamics of non-spherical particles.

4.2. Single particle statistics

When studying particle dynamics, the trajectories of individual particles can be followed, or the motion of groups of particles can be examined. In this paper we focus on single particles with varying aspect ratio released at different initial wall-normal positions and orientations. The study of single particles represents the first step in understanding particle behaviour in the system, and below results are presented for the particle translational and orientational dynamic properties.

Three particle aspect ratios are considered, representing disk-like ($\lambda = 0.1$), spherical ($\lambda = 1.0$), and needle-like ($\lambda = 10$) particles following the Loth (2008) classification, with these particles introduced into the flow to analyse the shape and orientation effect on particle behaviour. Note that $\lambda = 1.001$ was used rather than $\lambda = 1.0$ for the sphere in order to impose rotational dynamics which is only active for $\lambda \neq 1.0$. For a given particle relaxation time, τ_{eq}^+ , the particles have different aspect ratios, λ , and sphericity, Φ , but have

the same equivalent volume diameter, d_{ev} , mass and volume; this is different from other works (Zhang et al., 2001; Mortensen et al., 2008a, 2010; Tian et al., 2012) where for a given τ_{eq}^+ , the particles had different d_{ev} , mass and volume. In addition, three initial wall-normal locations are considered, at $x_{p0}^+ = 2, 8$ and 300 , corresponding to locations in the viscous sub-layer, the buffer layer and at the channel centre. The particles have fixed initial spanwise, $y^+ = 930$, and streamwise, $z^+ = 30$, locations. The shape and other relevant parameters of the particles considered are listed in Table 1. The simulations were performed in sets, with each set using three particles with the same relaxation time, τ_{eq}^+ , and equivalent diameter, d_{ev} , but with different aspect ratios, λ . Each set of simulations then employed the same initial conditions (particle initial position, orientation, velocity and spin). Hence, at the start of the runs, all the particles started with the same conditions and were subsequently subjected to the same turbulence field provided by the LES.

The point-wise approach of tracking particle trajectories is valid when the particle size is equal to or less than the smallest length scale, i.e. the Kolmogorov length scale. The Kolmogorov length scale for the flow considered is $\eta \sim 1.842 \times 10^{-4}$ m, and in wall units $\eta^+ \sim 2.763$. In this study the longest needle-like particle ($\tau_{eq}^+ = 125$, $\lambda = 10$) has a non-dimensional elongation ($2c^+$) slightly larger than the Kolmogorov length scale, although its equivalent volume diameter is $d_{ev}^+ = 0.619$. In terms of the latter equivalent diameter, all the particles considered were smaller than the Kolmogorov length scale. For the largest needle-like particles, therefore, the results are likely to be qualitatively accurate in terms of their trends, but less so from a quantitative viewpoint. Despite this limitation, previous research (Yin et al., 2004; Marchioli et al., 2010; Marchioli and Soldati, 2013; Njobuenwu and Fairweather, 2013b, 2014) routinely uses the point-wise approximation for particles with sizes beyond the smallest length scale to highlight such trends.

Results presented are in terms of the time evolution of the particle centroid in the wall-normal direction, x_p^+ , its orientation in terms of the direction cosines, $\cos \theta_x$, $\cos \theta_y$, $\cos \theta_z$, and its dynamic properties, e.g. incidence angle, α_i , Reynolds number, Re_p , and drag coefficient, C_D .

4.2.1. Spatial dynamics

To demonstrate the dynamic behaviour of particles in a turbulent channel flow, Fig. 8 shows a typical evolution of the spheroid (S1, S2, S3)=(disk, sphere, needle) trajectories in terms of their wall-normal distance with time for three different initial conditions ($x_{p0}^+ = 2, 8$ and 300). The results are based on $\tau_{eq}^+ = 125$ and an initial particle orientation ($\varphi_0 = 0, \theta_0 = 60^\circ, \psi_0 = 0$), implying the angle subtended between the particle's principal axis z' and its co-moving axis z'' is 60° . The trajectories were obtained for the same time interval, with the particles subjected to the same turbulence conditions.

It is clear that the disk-like particle with $\lambda < 0.1$ has the largest rate of dispersion when compared with the other particles for all three starting positions. This is expected following the recent observation (Njobuenwu and Fairweather, 2013b, 2014) where the oblate spheroid showed qualitatively higher dispersion than the other shapes for particles released from the channel centre at $x^+ = 300$. At $t^+ < \tau_{eq}^+$, the particle trajectories are approximately identical for the three particle shapes and for all initial release locations. However, at $t^+ \gg \tau_{eq}^+$ the various particles follow a different dispersion pattern, although the particles with $\lambda \geq 1.0$ remain reasonably close to one another, and for sufficiently large integration times after release the particles clearly loses any memory about their initial position and, hence, that position has a negligible effect on their long-time trajectory. Furthermore, it is interesting to note that the rate of the dispersion towards and away from the walls (at $x^+ = 0, 600$) in general increases with

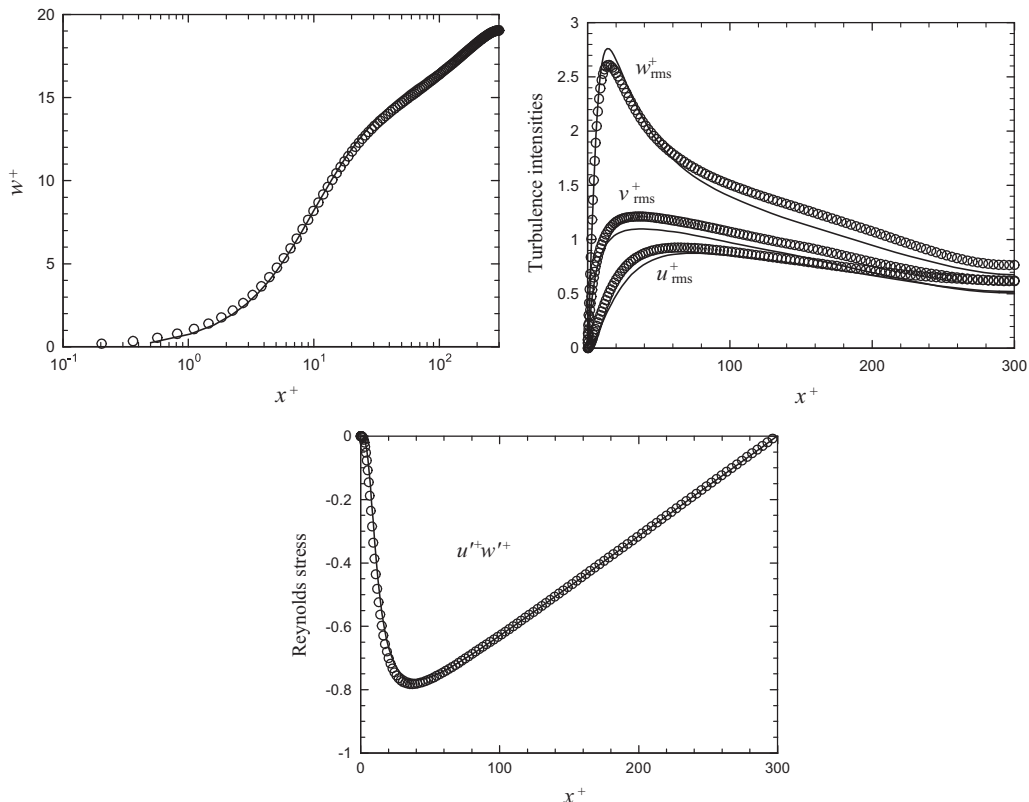


Fig. 7. Mean streamwise velocity (w^+), root-mean-square of components of velocity fluctuations ($u'_{rms} +$, $v'_{rms} +$ and $w'_{rms} +$), and Reynolds shear stress ($u'w'^+$). LES at $Re_t=300$ (solid lines) and DNS (Marchioli and Soldati, 2007) at $Re_t=300$ (symbols).

Table 1
Properties of super-quadric shapes investigated.

| Set | Shape | τ_{eq}^+ | λ | ρ_p/ρ | $a^+ = b^+$ | c^+ | d_{ev}^+ | $a^k = b^k$ | c^k | d_{ev}^k | Φ |
|-----|--------|---------------|-----------|---------------|-------------|-------|------------|-------------|-------|------------|--------|
| 1 | Disk | 5 | 0.1 | 769.2 | 0.737 | 0.074 | 0.342 | 0.267 | 0.027 | 0.124 | 0.418 |
| 2 | Sphere | 5 | 1.001 | 769.2 | 0.342 | 0.342 | 0.342 | 0.124 | 0.124 | 0.124 | 1.000 |
| 3 | Needle | 5 | 10 | 769.2 | 0.159 | 1.588 | 0.342 | 0.058 | 0.575 | 0.124 | 0.588 |
| 4 | Disk | 25 | 0.1 | 769.2 | 1.648 | 0.165 | 0.765 | 0.596 | 0.060 | 0.277 | 0.418 |
| 5 | Sphere | 25 | 1.001 | 769.2 | 0.765 | 0.765 | 0.765 | 0.277 | 0.277 | 0.277 | 1.000 |
| 6 | Needle | 25 | 10 | 769.2 | 0.355 | 3.550 | 0.765 | 0.128 | 1.285 | 0.277 | 0.588 |
| 7 | Disk | 125 | 0.1 | 769.2 | 3.685 | 0.368 | 1.710 | 1.334 | 0.133 | 0.619 | 0.418 |
| 8 | Sphere | 125 | 1.001 | 769.2 | 1.710 | 1.711 | 1.710 | 0.619 | 0.619 | 0.619 | 1.000 |
| 9 | Needle | 125 | 10 | 769.2 | 0.794 | 7.938 | 1.710 | 0.287 | 2.873 | 0.619 | 0.588 |

Note: Superscript k indicate variables made dimensionless with the Kolmogorov length scale. The Kolmogorov length scale is given by $\eta = (\nu^3/\epsilon)^{1/4}$, where ϵ is the average rate of dissipation of turbulence kinetic energy per unit mass, and ν is the kinematic viscosity of the fluid. Also, the computational time-step used, which is dependent on the grid resolution and the flow Reynolds number in wall units, is $\Delta t^+ \sim 0.049$ for both phases which is smaller than the smallest particle response time used which is $\tau_{eq}^+ = 5$.

the increasing non-sphericity of the particle. This phenomenon provides insight into the effect of particle aspect ratio on turbophoresis (preferential concentration). The dispersion patterns observed are therefore primarily due to a particle's rotational motion with respect to its aspect ratio, and as a secondary effect due to dispersion inherent with particle-pair motion. Jeffery (1922) also reported that particle rotation induced by shear may significantly affect particle trajectory.

In Fig. 9, the time evolution of the particle incidence angle, Reynolds number and drag coefficient for the three shaped particles with $\tau_{eq}^+ = 125$, all initially released at $x_{p0}^+ = 300$, is presented. Note that the α_i , Re_p and C_D in Fig. 9 produced the particle trajectories shown in Fig. 8(c). As expected in Fig. 9(a), the particle incidence angle that accounts for the particle orientation in the drag and profile lift forces varies from 0° to 180° . The incidence angle between the particle major axis direction (z') and the flow slip-velocity is determined for each time step, with the various particle

shapes exhibiting different incidence angles which clearly influence the particle motion because this affects the projected area normal to the directions of the drag and profile lift forces. The disk-shaped particle exhibits a wide range of more rapidly varying orientations compared to the needle-like and spherical particles, with the latter particle spending more time with a particular orientation.

In Fig. 9(b), particles with the same volume equivalent diameter have similar Reynolds numbers, but slight differences occur between the different shapes due to differences in the slip velocity which depends on the location of the particle centroid in the velocity gradient direction. The drag coefficient given in Fig. 9(c) is at most times different for the three particle shapes, with the needle-like particle having a reduced drag coefficient compared to the equivalent spherical particle, while the disk-shaped particle has in turn an increased drag relative to both other particle types. The time evolution of the particle incidence angle, Reynolds number and drag coefficient are not presented for single particles

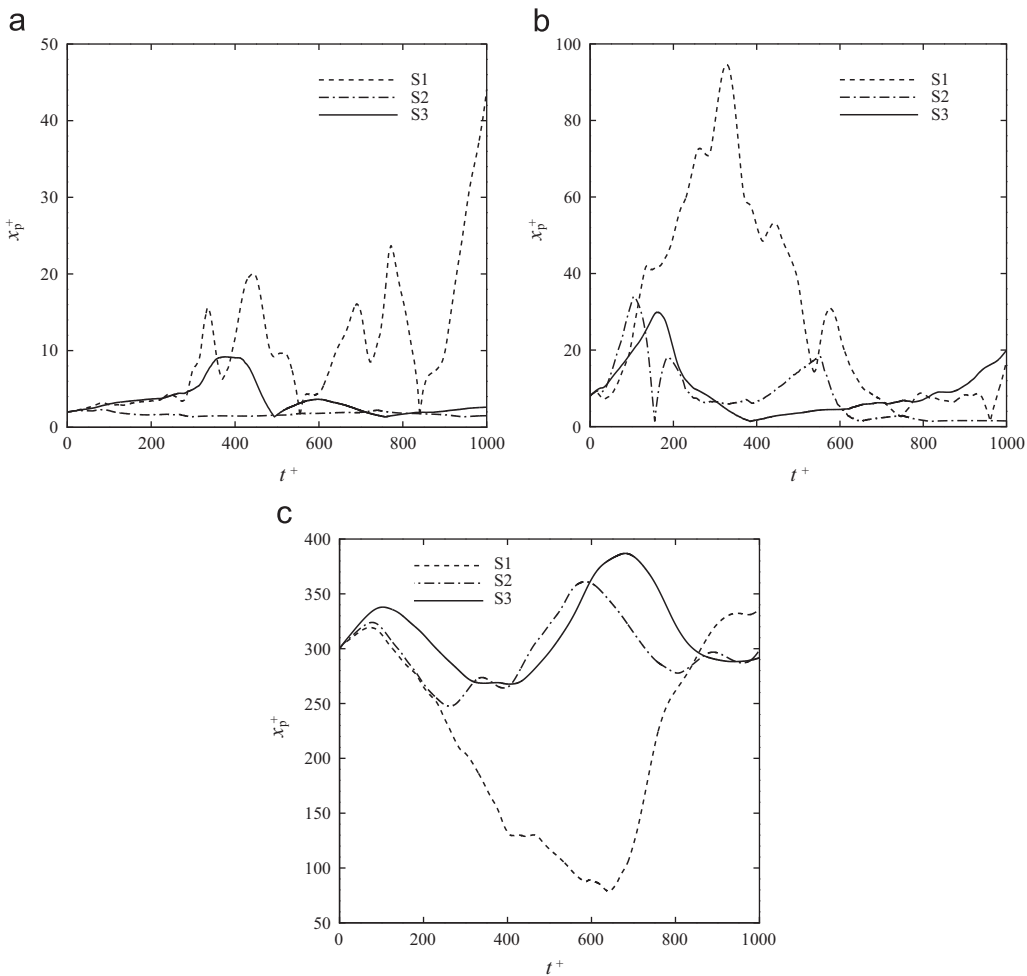


Fig. 8. Time evolution of the centroid of a single spheroidal particle for various initial release locations of its centroid from the wall, $x_{p0}^+ =$: (a) 2, (b) 8, and (c) 300. Series (S1, S2, S3)=Spheroids ($\lambda = 0.1, 1.0, 10.0$) and $\tau_{eq}^+ = 125$.

released in the near-wall region at $x_{p0}^+ = 2$ and 8 since, due to the complexity of the resulting plots, it was impossible to establish any trends with respect to particle shape. In addition, evaluation of these dynamic properties at lower particle relaxation time did not reveal any trends significantly different from those shown in Fig. 9.

The effect of particle inertia on trajectory, measured by the particle non-dimensional relaxation time (also called particle Stokes number), is shown in Fig. 10. Each figure gives the trajectories of particles of the same shape that are released from the same wall-normal location, $x_{p0}^+ = 300$, with the series (S1, S2, S3) representing the particle relaxation times ($\tau_{eq}^+ = 5, 25, 125$). It is clear from these results that in general all the various particle shapes exhibit similar trends with respect to the particle relaxation time. The smaller particles follow the fluid motion relatively well with a high dispersion rate, whereas the particles with the highest inertia show a lower dispersion rate and a damping of the effect of the fluid's fluctuating motion. This behaviour is due to the particle inertia filtering out some of the effects of the local flow, making large particles relatively insensitive to small-scale velocity fluctuations.

A clearer illustration of this effect is provided by plots of the square of the displacement of the particle centroid, $\sigma_x = (x_p^+ - x_0^+)^2 / Re_\tau^2$, given in Fig. 11 for the various particle shapes, where the lower inertia particles in general again show higher displacement values. The results of Fig. 11 further confirm the well-known result that particles with large relaxation times are less sensitive to small-scale turbulent structures (ElMaihy and Nicolleau, 2005) and that, in the absence of gravity, a particle disperses in an

isotropic turbulence field with departures from fluid particle paths largely due to the inertial effect. The only slight exception to these conclusions are for the disk-shaped particles, where the $\tau_{eq}^+ = 5$ and 25 particles exhibit a similar level of dispersion, and for the spherical particles, where the higher inertia $\tau_{eq}^+ = 25$ and 125 particles both display reduced dispersion relative to the $\tau_{eq}^+ = 5$ case.

Overall, the results of Figs. 8, 10 and 11 demonstrate that particle shape (and orientation), inertia and initial position all affect the temporal behaviour of a particle in a turbulent channel flow. They demonstrate that at small times, $t^+ < \tau_{eq}^+$, the particles move approximately with linear paths, hence their trajectories and dispersion patterns look similar irrespective of their shape, inertia and initial position. This is expected particle behaviour for times less than the Lagrangian integral time scale since, when a particle is set in motion by the velocity fluctuations, it moves steadily in a certain direction at a certain speed, with its motion becoming diffusive-like as the integral time scale is approached. The length of this time period depends, however, on the particle inertia. As shown in Figs. 10 and 11, the duration for which a particle maintains a seemly straight-line trajectory increases with its inertia, and this can be attributed to the fact that particles with higher inertia take a longer time to overcome the influence of their initial conditions. Hence, to obtain particle statistics devoid of the effect of initial conditions, sampling must be performed at $t^+ \gg \tau_{eq}^+$. Also, when the three shapes of particle are released from the same wall-normal location they do not migrate to the same distance from the wall

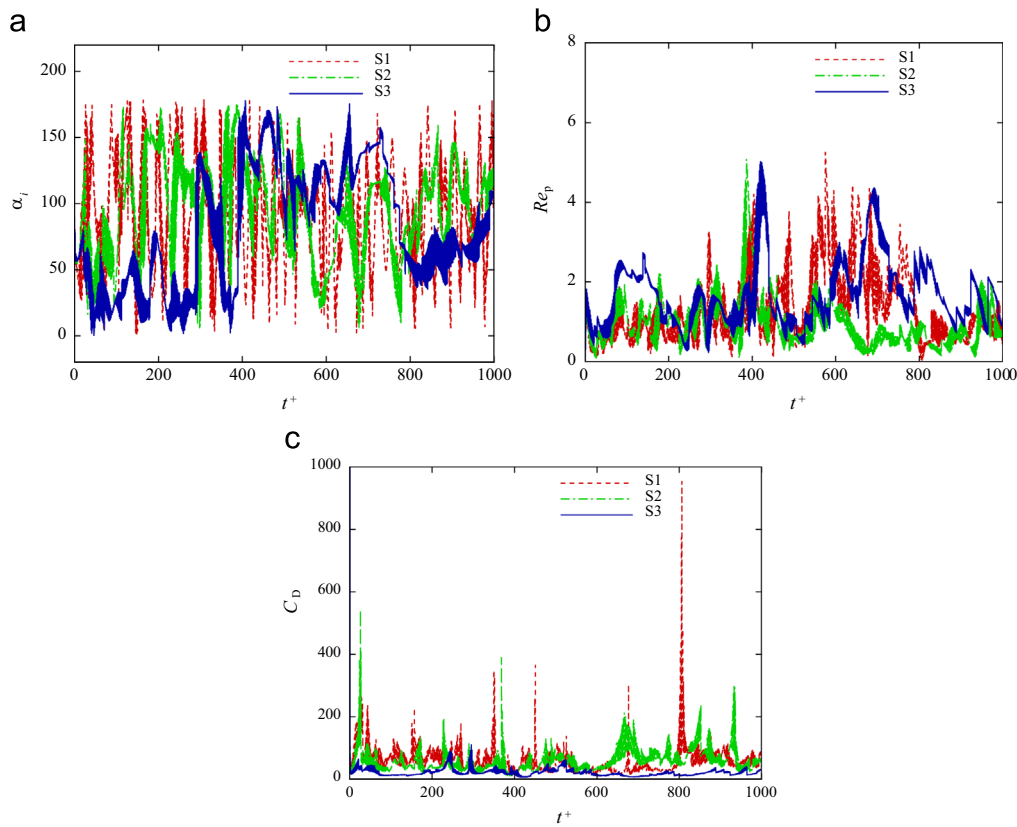


Fig. 9. Time evolution of: (a) incidence angle between particle relative velocity and particle major axis z' , (b) Reynolds number, and (c) drag coefficient for various particle shapes. Series (S1, S2, S3)=Spheroids ($\lambda = 0.1, 1.0, 10.0$), $\tau_{eq}^+ = 125$ and $x_{p0}^+ = 300$.

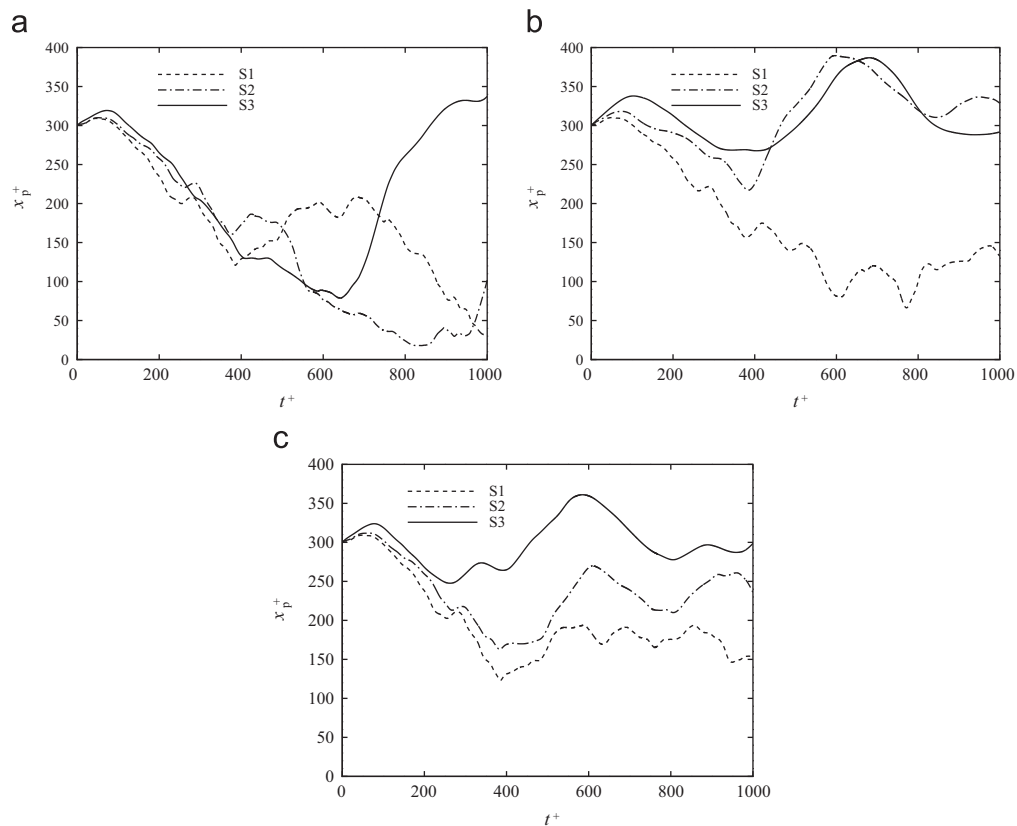


Fig. 10. Time evolution of the centroid of a single spheroidal particle for various particle relaxation times: (a) disk-shaped, (b) spherical, and (c) needle-like particles. Series (S1, S2, S3)=particle relaxation time ($\tau_{eq}^+ = 5, 25, 125$) and $x_{p0}^+ = 300$.

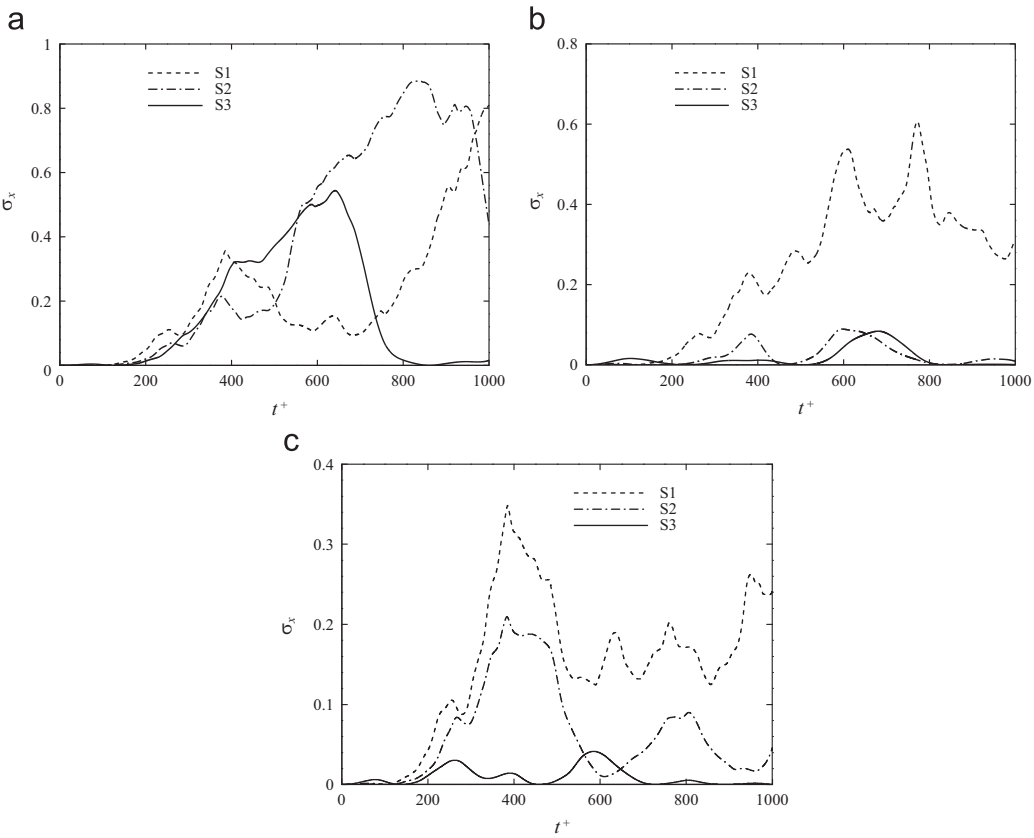


Fig. 11. Time evolution of the square of the displacement of the centroid of a single spheroidal particle for various particle relaxation times: (a) disk-shaped, (b) spherical, and (c) needle-like particles. Series (S1, S2, S3)=particle relaxation time ($\tau_{eq}^+ = 5, 25, 125$) and $x_{p0}^+ = 300$.

over the time period examined, with a continuous transverse migration taking place such that they eventually forgot their initial position. This contrasts with Broday et al. (1998) observation where, in a vertical Poiseuille flow, a spheroidal particle was found to arrive at an equilibrium position in the flow cross-section, independent of the particle's initial cross-sectional location.

Again, it should be noted that the trends observed in Figs. 10 and 11 were not significantly affected when particles were released from wall-normal positions of $x_{p0}^+ = 2$ and 8.

4.2.2. Orientational dynamics

The results in this section focus on the orientation of the non-spherical particle due to its rotation, where the orientation is characterised by the direction cosines the particle principal axis, z' , makes with the axes of the co-moving frame, \mathbf{x}' , which is always parallel to the inertial frame \mathbf{x} . In the configuration used for the inertial co-ordinate \mathbf{x} (see Fig. 1 and 3), the streamwise direction of the channel flow is along the z -axis, while the velocity gradient (wall-normal) and the vorticity (spanwise) are orientated in the x - and y -directions, respectively. The direction cosines, $\cos \theta_x$, $\cos \theta_y$ and $\cos \theta_z$, represent the particle orientation with respect to the particle co-moving axes x'' , y'' and z'' , respectively, subject to the constraint $\cos^2 \theta_x + \cos^2 \theta_y + \cos^2 \theta_z = 1$ (see illustration in Fig. 2 (c)). Obviously, $\cos \theta_x = 0$ with $\theta_x = 90^\circ$ means that the particle principal axis is perpendicular to the particle co-moving axis x'' , while for $\cos \theta_x = 1$ with $\theta_x = 0^\circ$ the particle aligns with the co-moving axis x'' . The same analogies apply to the remaining two particle co-moving axes, y'' and z'' . The particle orientation cannot be well understood in isolation, but must be considered in relation to its spatial location since the particle's position in the velocity gradient direction gives an indication of the turbulence intensity and

velocity gradient that it experiences. For a channel flow, the mean velocity gradient is smaller in the vicinity of the channel centre than in the near-wall region. Therefore, the orientation of the anisotropic particles with respect to the flow is due to the interplay between the randomizing process of turbulence and the local velocity gradients. Below the effect of particle inertia and shape on their orientation with time is considered. The particle initial orientation, specified by the Euler angles $(\phi_0, \theta_0, \psi_0) = (0^\circ, 60^\circ, 0^\circ)$, is kept constant, with the particle shape ($\lambda = 0.1, 1.0$ and 10.0) and relaxation time ($\tau_{eq}^+ = 5, 25$ and 125) varied.

The time evolution of the direction cosines (S1, S2, S3)= $(\cos \theta_x, \cos \theta_y, \cos \theta_z)$ for the three particle shapes considered and a particle inertia $\tau_{eq}^+ = 5$ is shown in Fig. 12, with the results of Fig. 12(a–c) being for the disk-shaped particle, Fig. 12(d–f) for the spherical particle and Fig. 12(g–i) for the needle-like particle. Results for particles released at wall-normal locations of $x_{p0}^+ = 2, 8$ and 300, demonstrating the effect of velocity gradient on particle orientation, are also considered. Initial Euler angles of $(\phi_0, \theta_0, \psi_0) = (0^\circ, 60^\circ, 0^\circ)$ correspond to initial particle directional angles of $(\theta_{x0}, \theta_{y0}, \theta_{z0}) = (0^\circ, 135^\circ, 60^\circ)$, giving initial direction cosines of $(\cos \theta_{x0}, \cos \theta_{y0}, \cos \theta_{z0}) = (0, -0.7071, 0.5)$. Also note that θ_{z0} is the angle between the particle principal axis z' and z'' , hence, $\theta_{z0} = \theta_0$ at $t^+ = 0$. Within the time range $0 < t^+ < 1000$ of the simulations, the transient particle orientation demonstrates different rotational modes.

Usually turbulence is thought of as a randomizing process, and that any particles carried along with a turbulent flow will have random orientations as a consequence. However, the velocity gradients in turbulence have the net effect of aligning anisotropic particles with the inertial co-ordinate system. A non-spherical particle settling in a stagnant fluid therefore maintains a steady orientation in the Stokes limit (Yin et al., 2003). For the disk in

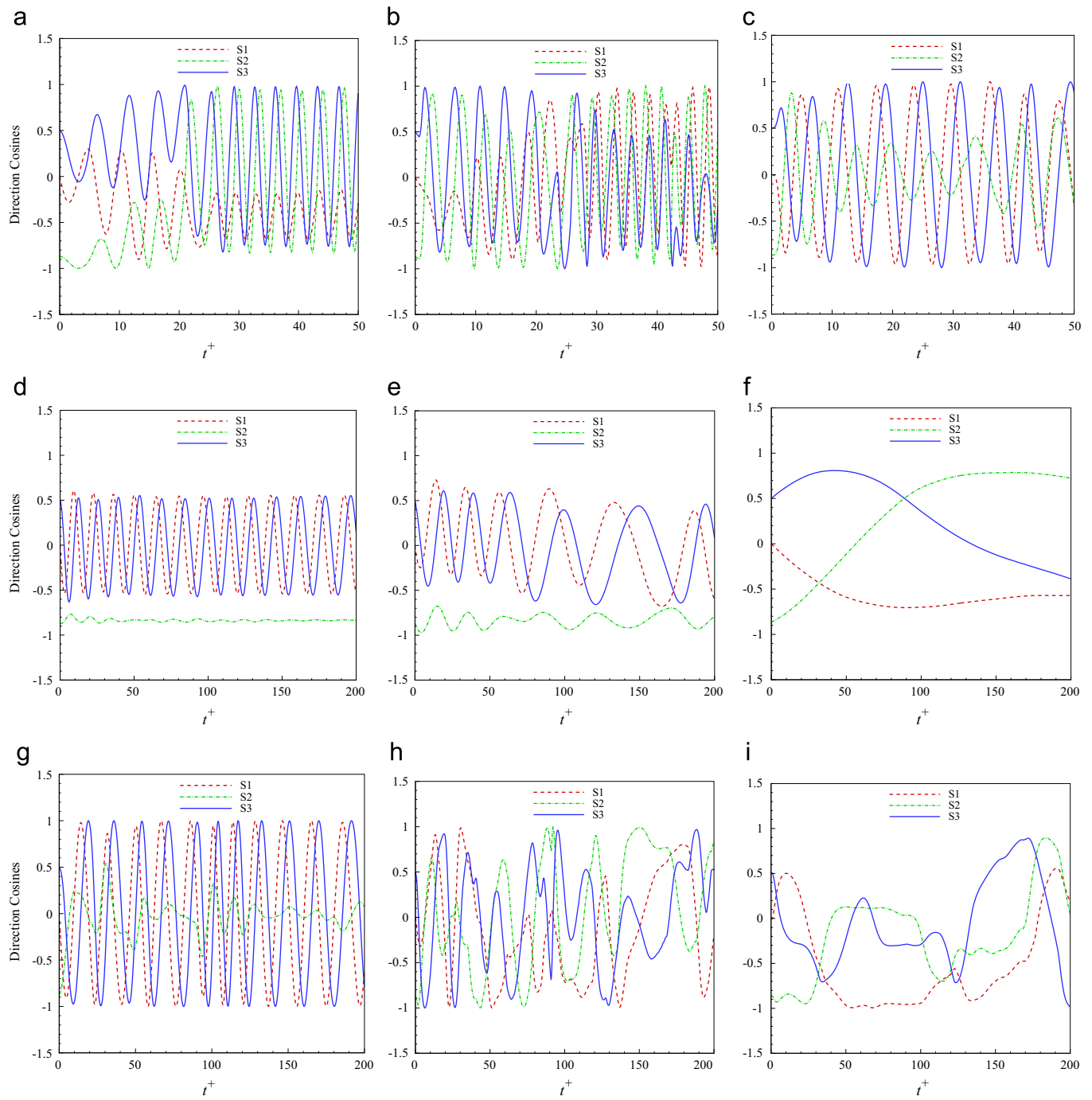


Fig. 12. Time evolution of the direction cosines of the z' -axis with respect to the x -, y - and z -axes of the disk-shaped (a–c), spherical (d–f) and needle-like (g–i) particles as a function of particle initial position, $x_{p0}^+ =$: (a, d, g) 2, (b, e, h) 8, and (c, f, i) 300. Series (S_1, S_2, S_3) = ($\cos \theta_x, \cos \theta_y, \cos \theta_z$) and $\tau_{eq}^+ = 5$.

Fig. 12(a)–(c), only orientation profiles up to $t^+ = 50$ are shown in the interests of clarity since beyond this time the plots are sufficiently complex to be difficult to read. However, the orientation profiles at greater times are considered later.

After some disturbance arising from the initial conditions, the disk is seen to take up an almost stable rotation with respect to the three directions, i.e. the x -, y - and z -axes. The principal axis of the disk (z' -axis) has no preferential alignment to the inertial co-ordinate regardless its initial position, but the disk is rotating in all three directions. The wave height of the orientation profile of the disk is the same with respect to the y - and z -axes in Fig. 12(a), initially with respect to the y - and z -axes and later the x - and y -axes in Fig. 12(b), and with respect to x - and z -axes in Fig. 12(c). The profiles with

equal wave height have their troughs and peaks at approximately -1 and 1 , respectively. The direction cosine $\cos \theta_x$, following initial disturbances, oscillates about -0.5 , and moving from left to right in Fig. 12(a)–(c), the number of cycles per unit time decreases. This implies that a disk shaped particle with a small relaxation time is always rotating in all directions, with the orientation periodic in time when in the viscous sub-layer region (Fig. 12(a)). The behaviour in this region mimics the laminar flow behaviour noted in Jeffery's analysis (Jeffery, 1922) and by Yin et al. (2003).

In Fig. 12(d)–(f) results for the spherical particle demonstrate that its orientation at all distances from the solid surface is more stable than that of the disk considered in Fig. 12(a)–(c). Close to the surface, the particle exhibits the precessing and nutating mode, as

noted by Huang et al. (2012) for a prolate spheroid at $Re = 120$. The wave height of the orientation profile of this particle is shorter than was obtained for the disk, with $\cos \theta_x$ and $\cos \theta_z$ changing periodically in the range -0.5 and 0.5 for the particle injected at $x_{p0}^+ = 2$, and with $\cos \theta_y$ remaining almost unchanged from its initial orientation of $\cos \theta_y = -0.71$ ($\theta_y = 135^\circ$) throughout the time range considered. In Fig. 12(e), the particle injected in the buffer region at $x_{p0}^+ = 8$ shows changes in both its wave amplitude and frequency, with both increasing with time. This demonstrates that for this relaxation time, the particle is sensitive to the fluid velocity scale, with its rotation influenced by the fluid velocity gradient and turbulent fluctuations and, hence, the particle rotates with the flow. The precessing and nutating mode was again exhibited in this case, however, the orientation of the sphere's principal z' -axis with respect to the vorticity y' -axis showed some

form of periodicity. At the channel centre, Fig. 12(f), the spherical particle shows a highly periodic orientation in all directions with a larger amplitude and period than for the other release locations considered. This demonstrates that the fluid, and hence particle, rotation at this location is not biased in any of the three directions, and strengthens the argument that the particle orientation is largely dependent on its position in the wall-normal direction, especially for particles with small relaxation times. Broadly, for the spherical particle therefore, as the release location moves away from the wall the period of orientation increases from the viscous to the free stream regions. The orientation of the needle-like particle shown in Fig. 12(g)–(i) is clearly less stable than that of the disk or spherical particles. The needle-like particle injected at $x_{p0}^+ = 2$ in Fig. 12(g) shows two components of its orientation that are periodic in time, with equal nutation amplitudes of $-1 < \cos \theta_x < 1$ and

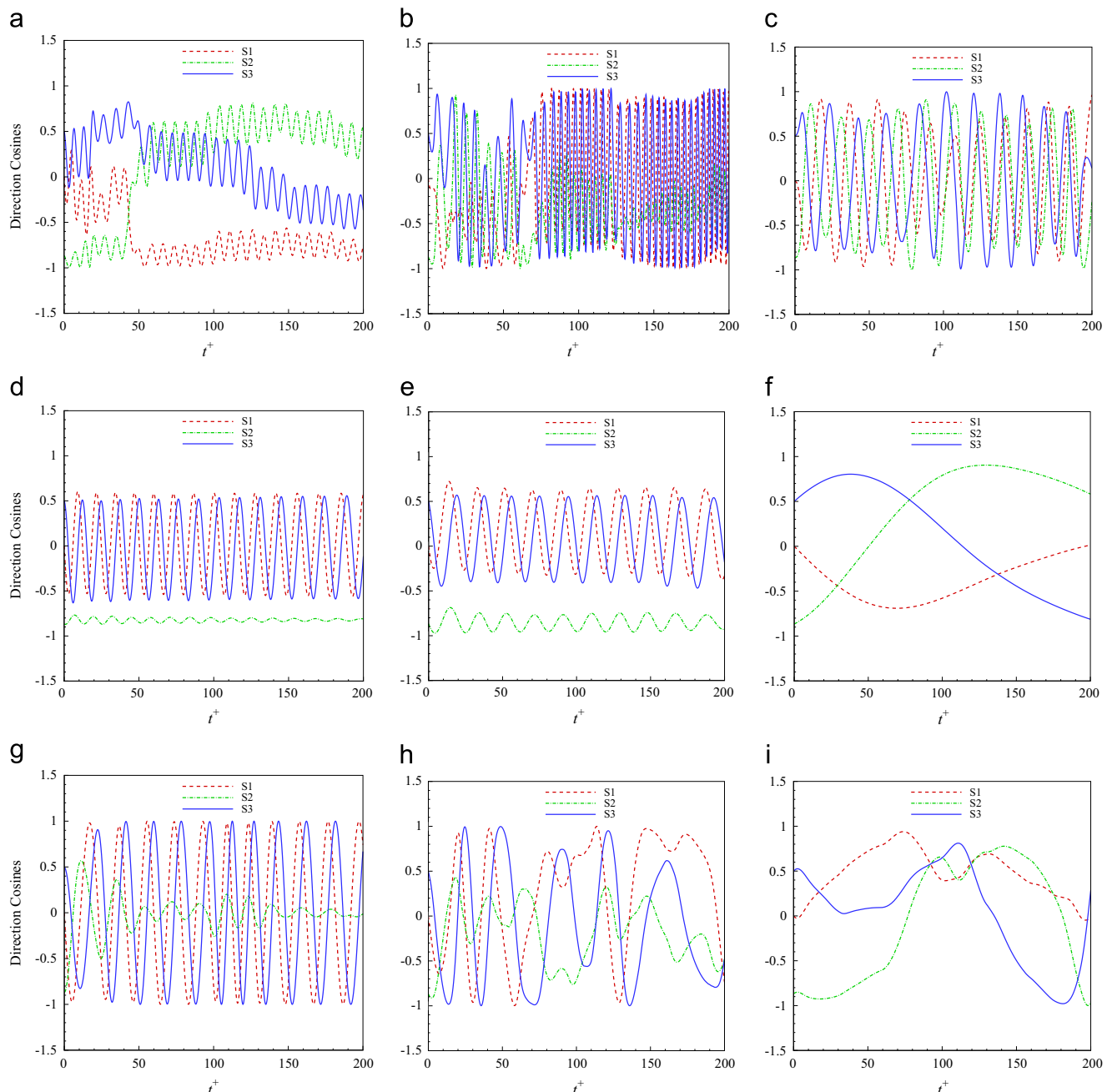


Fig. 13. Time evolution of the direction cosines of the z' -axis with respect to the x -, y - and z -axes of the disk-shaped (a, b, c), spherical (d–f), and needle-like (g–i) particles as a function of particle initial position, $x_{p0}^+ =$ (a, d, g) 2, (b, e, h) 8, and (c, f, i) 300. Series (S1, S2, S3) = $(\cos \theta_x, \cos \theta_y, \cos \theta_z)$ and $\tau_{eq}^+ = 25$.

$-1 < \cos \theta_z < 1$. The needle is rotating in the (x, z) -plane and, although its principal z' -axis is less defined, it eventually aligns with the vorticity axis where θ_y averages to 0° . The orientations of the needle particle injected in the buffer region given in Fig. 12(h), and at the channel centre in Fig. 12(i), are more complex than observed previously, with the various orientations displaying multiple frequencies and amplitudes with time. This is caused by the large dispersion of this particle, as noted earlier, with the particle moving from one turbulent region to another with time.

The orientation of the disk principal z' -axis with respect to the inertial frame x -, y - and z -axes for a moderate particle relaxation time, $\tau_{eq}^+ = 25$, as a function of the non-dimensional time, t^+ , is shown in Fig. 13(a)–(c). The disk injected in the near-wall region shown in Fig. 13(a) interacted with the wall at $x^+ = 0$ just before $t^+ = 50$, with that interaction altering the angular momentum of

the disk, giving rise to a jump in the amplitudes of the orientation. Following this jump, the disk precesses around the x -axis with a nutation, although this is more complex than observed in Fig. 12(a) for the low particle relaxation time. The period of the orientation in the three directions is similar, but the nutation amplitude increases in the x -, y - and z -directions. The disk injected in the buffer region, the results for which are shown in Fig. 13(b), and at the channel centre in Fig. 13(c), shows orientations similar to the $\tau_{eq}^+ = 5$ case in Fig. 12(b) and (c). Comparing the direction cosines ($S1, S2, S3$) = $(\cos \theta_x, \cos \theta_y, \cos \theta_z)$ of the $\tau_{eq}^+ = 25$ spherical particle in Fig. 13(d–f) and the $\tau_{eq}^+ = 5$ particle in Fig. 12(d)–(f), there are similarities between both sets of results for all three initial particle positions. It is therefore clear that the orientational dynamics of the spherical particle are less dependent on the particle inertia but largely on the particle position in the velocity gradient

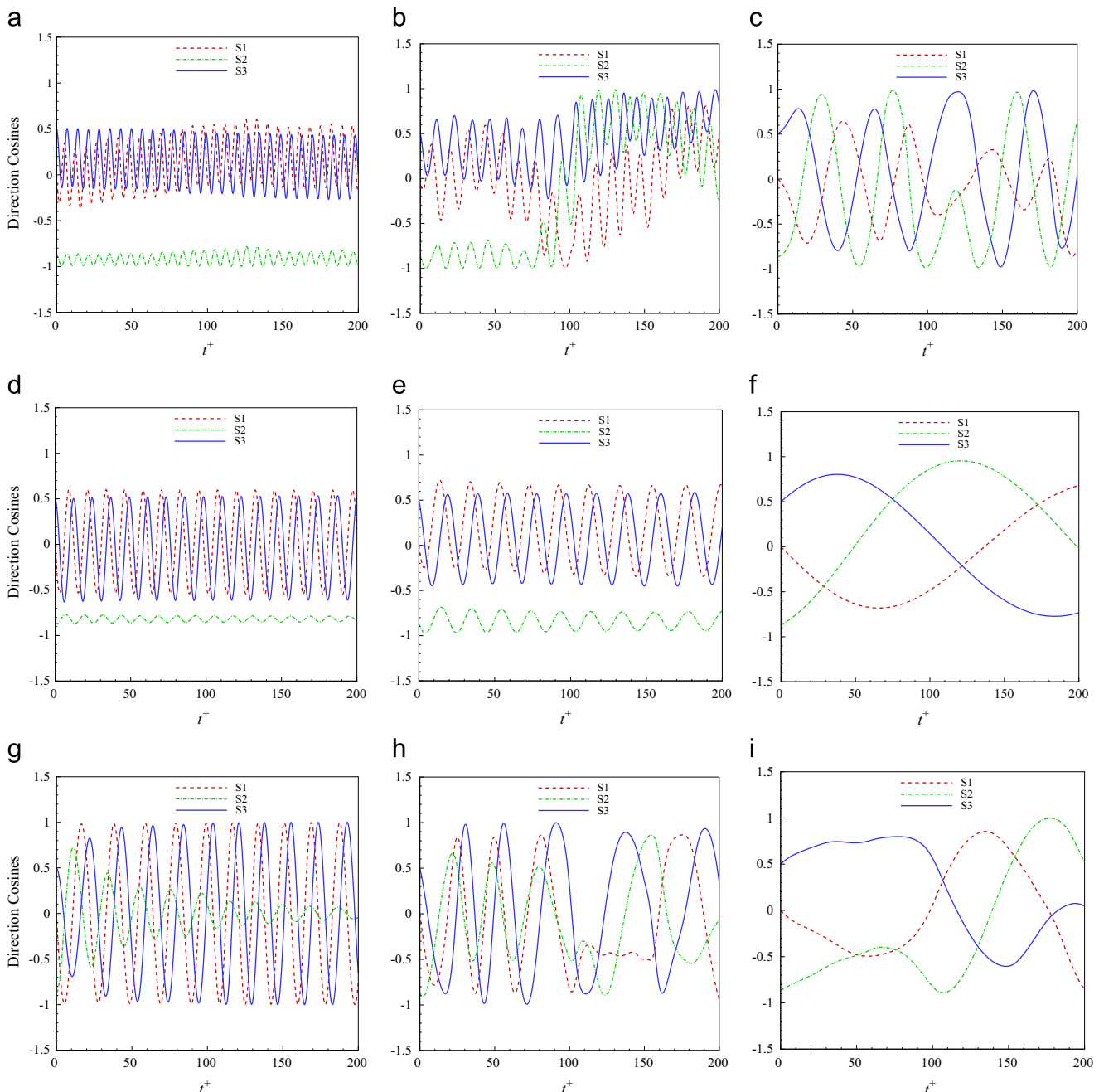


Fig. 14. Time evolution of the direction cosines of the z' -axis with respect to the x -, y - and z -axes of the disk-shaped (a, b, c), spherical (d–f) and needle-like (g–i) particles as a function of particle initial position, $x_{p0}^+ =$: (a, d, g) 2, (b, e, h) 8, and (c, f, i) 300. Series ($S1, S2, S3$) = $(\cos \theta_x, \cos \theta_y, \cos \theta_z)$ and $\tau_{eq}^+ = 125$.

direction. The orientation of the $\tau_{eq}^+ = 25$ needle-like particle injected in the viscous sub-layer given in Fig. 13(g) again shows a close similarity to the orientation of the $\tau_{eq}^+ = 5$ particle in Fig. 12(g). Complex orientations are observed for the $\tau_{eq}^+ = 25$ needle injected in the buffer region in Fig. 13(h), with a transition from one nutation amplitude to another as the needle transverses from one velocity gradient position to another. The nutation amplitude in the x - and z - directions at most times varies from -1 to 1 , and is larger than that in the y -direction. The $\tau_{eq}^+ = 25$ needle injected at the channel centre, Fig. 13(i), again exhibits different frequencies, and this trend continues with further increases in the particle relaxation time (as below). Huang et al. (2012) also reported a similar trend, with many orientation frequencies observed with increases with Re .

Simulation results for a $\tau_{eq}^+ = 125$ disk-shaped particle injected at $x_{p0}^+ = 2$ given in Fig. 14(a) shows that the particle orientation in all three directions is periodic with time. Its principal z' -axis precesses around the vorticity y -axis, while the nutation amplitude in the x - and z -directions changes with time from -0.5 to 0.5 . In Fig. 14(b) the orientation of the principal z' -axis with respect to the velocity gradient x -axis and the vorticity y -axis show jumps in their amplitude as the disk transverses different boundary layer positions. The disk injected at the channel centre in Fig. 14(c) shows a relatively steady rotation as the particle remained within this region of the boundary layer over the time interval considered. In Fig. 14(d)–(f), the orientational behaviour in all three directions of the $\tau_{eq}^+ = 125$ spherical particle mimics that of the $\tau_{eq}^+ = 25$ case shown

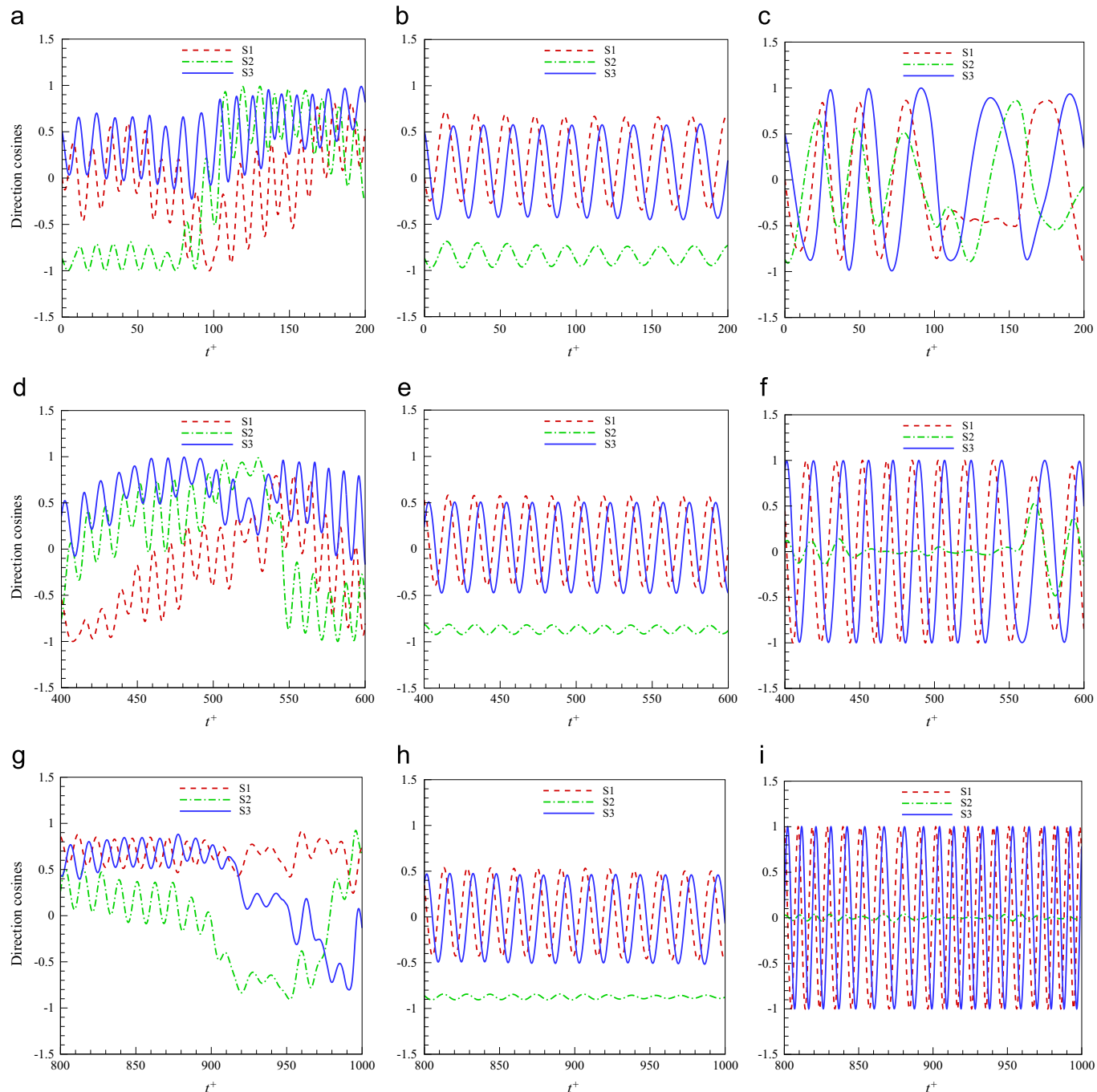


Fig. 15. Time evolution of the direction cosines of the z' -axis with respect to the x -, y - and z -axes of the disk-shaped (a, d, g), spherical (b, e, h) and needle-like (c, f, i) particles at (a–c) $0 \leq t^+ \leq 200$, (d–f) $400 \leq t^+ \leq 600$, and (g–i) $800 \leq t^+ \leq 1000$. Series $(S1, S2, S3) = (\cos \theta_x, \cos \theta_y, \cos \theta_z)$, $\tau_{eq}^+ = 125$ and $x_{p0}^+ = 8$.

in Fig. 13(d)–(f). The $\tau_{eq}^+ = 125$ needle-like particle results given in Fig. 14(g)–(i) exhibit a tumbling mode, with both the orientational amplitude and frequency of the direction cosines found to be close to that of $\tau_{eq}^+ = 25$ case shown in Fig. 13(g)–(i).

Lastly, the time evolution of the direction cosines showing the orientational dynamics of a single disk, sphere and needle with $\tau_{eq}^+ = 125$ released in the buffer region for the time interval $t^+ \leq 1000$, previously reported in terms of their spatial dynamics in Fig. 8, is shown Fig. 15. Based on the criteria defined in Huang et al. (2012) and the discussions above, the disk in Fig. 15(a), (d) and (g) exhibits many frequencies and amplitudes in all the three time intervals reported. This is expected as the disk injected in the buffer region, shown in Fig. 8(b), transverses across the boundary layer, with the velocity gradient at each boundary layer location affecting its orientation frequency and amplitude. The spherical particle, Fig. 15(b), (e) and (h), enters a periodic mode at the outset and remains stable throughout the reported simulation time. The orientation of this particle shows a similar frequency and amplitude for $\cos \theta_x$ and $\cos \theta_z$ irrespective of its initial release location. The spherical particle is rotating in the (x, z) -plane, and its principal z' -axis eventually stops rotating along the vorticity axis, where θ_y ultimately averages to its initial value of 135° . The $\tau_{eq}^+ = 125$ needle released at $x_0^+ = 8$, shown in Fig. 15(c), (f) and (i), experiences some complex orientations initially but maintains a periodic orientation at time $t^+ > 200$ with respect to the streamwise and velocity gradient axes. Its principal axis eventually aligns with the vorticity y axis, where θ_y evolves to 0° at times $t^+ > 800$.

5. Conclusions

A computational approach for simulating the three-dimensional motion of single non-spherical particles in a turbulent channel flow has been described, assuming one-way coupling between the fluid and the particles. The approach involves the complete numerical simulation of the particles' translational and orientational behaviour in a fully developed turbulent flow field obtained using large eddy simulation coupled to a Lagrangian particle tracking algorithm and Euler's law of rotational motion. The technique is general and can be applied to any regular isotropic non-spherical particle, and in the present study, results were presented for ellipsoidal particles (disk-shaped, spherical and needle-like) in the Stokesian and Newtonian regimes, with the work described providing an extension to previous studies that use Jeffery's equations to model drag force and hydrodynamic torque. In wall-bounded turbulence, it has been demonstrated that the particle linear and rotational dynamics are affected by the fluid shear rate, and particle inertia and shape, as well as the initial position and orientation of the particles. At small times, the particles move approximately with linear paths, with their dispersion patterns similar irrespective of their shape, inertia and initial position. The length of this time period depends on the particle inertia, although beyond this period different shapes of particle do not migrate to the same distance from the wall over the simulation times examined. Particle orientation was characterised using the direction cosine of the particle principal z' -axis with respect to the inertial x , y and z axes. The results show that turbulent dispersion forces non-spherical particles to have a broad orientation distribution. Velocity gradient, aspect ratio, particle inertia and initial orientation all have an effect on the alignment of the particle principal axis to the inertial axes. Disk-shaped particles with small relaxation times are always in rotation in all directions, and the orientation is periodic in time when the particle is injected in the viscous sub-layer and at the channel centre. A change in the orientation state was observed when the disk was injected in the buffer region. At higher relaxation times, interactions with the wall and translation through the boundary layer caused

jumps in the amplitude of the orientation, and a subsequent precessing and nutating orientation state. For the spherical particle, the orientation behaviour in all three directions, which is independent of the particle relaxation time, exhibits the tumbling mode, and both the orientational amplitude and frequency of the direction cosines are found to be similar at all particle relaxation times. The orientation of the needle-like particle is less stable than that of the disk and sphere, and at lower relaxation times exhibits complex orientation profiles, although the stability of these particles increases at higher relaxation times.

The overall objective of the work described was to study the behaviour of single particles of different shapes and sizes, and their translational and orientational behaviour in a turbulent channel flow. To that end, all the different shaped particles were tracked through the same turbulent flow field having been released from the same wall-normal locations in order to ensure consistency in comparing the results obtained. Clearly many issues remain, for example the influence of the spanwise release location on particle behaviour and, for particles close to the wall, the position of that location relative, for example, to the coherent structures which give rise to ejection and sweep events which play a role in determining that behaviour. Given the instantaneous and spatially varying nature of such events, however, the only meaningful way to investigate their influence is through the use of multiple particles released at different spanwise locations and averaged over time and space. These and related issues will be addressed in future work on the dynamics of multiple particles in a turbulent channel flow. Lastly, a point-wise approximation was adopted for the larger particles ($\tau_{eq}^+ = 125$, $\lambda = 10$) even though their longest characteristic length is greater than the smallest Kolmogorov length scale (although the equivalent volume diameter in all cases was smaller than that length scale). Whilst the use of such an approximation is reasonable and common practice amongst various authors (Yin et al., 2004; Marchioli et al., 2010; Marchioli and Soldati, 2013; Njobuenwu and Fairweather, 2013b, 2014), this simplification should be relaxed in future work.

Acknowledgements

The authors wish to thank the Engineering and Physical Sciences Research Council for their financial support of the work reported in this paper under EPSRC Grant EP/I003010/1, "Computational Modelling for Advanced Nuclear Power Plants".

References

- Armenio, V., Piomelli, U., Fiorotto, V., 1999. Effect of the subgrid scales on particle motion. *Phys. Fluids* 11, 3030–3042.
- Besnard, D., Harlow, F.H., 1986. Nonspherical particles in two-phase flow. *Int. J. Multiph. Flow* 12, 891–912.
- Bini, M., Jones, W., 2007. Particle acceleration in turbulent flows: a class of nonlinear stochastic models for intermittency. *Phys. Fluids* 19, 035104.
- Bini, M., Jones, W.P., 2008. Large-eddy simulation of particle-laden turbulent flows. *J. Fluid Mech.* 614, 207–252.
- Brenner, H., 1963. The Stokes resistance of an arbitrary particle. *Chem. Eng. Sci.* 18, 1–25.
- Brenner, H., 1964. The Stokes resistance of an arbitrary particle – IV Arbitrary fields of flow. *Chem. Eng. Sci.* 19, 703–727.
- Broday, D., Fichman, M., Shapiro, M., Gutfinger, C., 1998. Motion of spheroidal particles in vertical shear flows. *Phys. Fluids* 10, 86–100.
- Carlsson, A., Söderberg, L.D., Lundell, F., 2006. Fiber orientation control related to papermaking. *J. Fluids Eng.* 129, 457–465.
- Chhabra, R.P., Agarwal, L., Sinha, N.K., 1999. Drag on non-spherical particles: an evaluation of available methods. *Powder Technol.* 101, 288–295.
- Chien, S.F., 1994. Settling velocity of irregularly shaped particles. *SPE Drill. Complet.* 9, 281–289.
- Cox, R.G., 1971. The motion of long slender bodies in a viscous fluid. Part 2. Shear flow. *J. Fluid Mech.* 45, 625–657.

- Dearing, S., Campolo, M., Capone, A., Soldati, A., 2012. Phase discrimination and object fitting to measure fibers distribution and orientation in turbulent pipe flows. *Exp. Fluids* 54, 1–14.
- di Mare, L., Jones, W.P., 2003. LES of turbulent flow past a swept fence. *Int. J. Heat Fluid Flow* 24, 606–615.
- Ding, E.J., Aidun, C.K., 2000. The dynamics and scaling law for particles suspended in shear flow with inertia. *J. Fluid Mech.* 423, 317–344.
- ElMaihy, A., Nicolleau, F., 2005. Investigation of the dispersion of heavy-particle pairs and Richardson's law using kinematic simulation. *Phys. Rev. E* 71, 046307.
- Fan, F.-G., Ahmadi, G., 1995. A sublayer model for wall deposition of ellipsoidal particles in turbulent streams. *J. Aerosol Sci.* 26, 813–840.
- Feng, J., Hu, H.H., Joseph, D.D., 1994. Direct simulation of initial value problems for the motion of solid bodies in a Newtonian fluid. Part 2. Couette and Poiseuille flows. *J. Fluid Mech.* 277, 271–301.
- Ganser, G.H., 1993. A rational approach to drag prediction of spherical and nonspherical particles. *Powder Technol.* 77, 143–152.
- Germano, M., Piomelli, U., Moin, P., Cabot, W.H., 1991. A dynamic subgrid-scale eddy viscosity model. *Phys. Fluids A* 3, 1760–1765.
- Glowinski, R., Pan, T.W., Hesla, T.I., Joseph, D.D., 1999. A distributed Lagrange multiplier/fictitious domain method for particulate flows. *Int. J. Multiph. Flow* 25, 755–794.
- Glowinski, R., Pan, T.W., Hesla, T.I., Joseph, D.D., Périaux, J., 2001. A fictitious domain approach to the direct numerical simulation of incompressible viscous flow past moving rigid bodies: application to particulate flow. *J. Comput. Phys.* 169, 363–426.
- Goldstein, H., 1980. Classical Mechanics, 2nd ed. Addison-Wesley, Reading, MA.
- Haider, A., Levenspiel, O., 1989. Drag coefficient and terminal velocity of spherical and nonspherical particles. *Powder Technol.* 58, 63–70.
- Hakansson, K.O., Kvick, M., Lundell, F., Prahl Wittberg, L., Söderberg, L.D., 2013. Measurement of width and intensity of particle streaks in turbulent flows. *Exp. Fluids* 54, 1–13.
- Hartman, M., Trnka, O., Svoboda, K., 1994. Free settling of nonspherical particles. *Ind. Eng. Chem. Res.* 33, 1979–1983.
- Hazelton, R., 1987. Characteristics of fuel crud and its impact on storage, handling, and shipment of spent fuel.
- Hilton, J.E., Cleary, P.W., 2011. The influence of particle shape on flow modes in pneumatic conveying. *Chem. Eng. Sci.* 66, 231–240.
- Holm, R., Söderberg, D., 2007. Shear influence on fibre orientation. *Rheol. Acta* 46, 721–729.
- Huang, H., Yang, X., Krafczyk, M., Lu, X.-Y., 2012. Rotation of spheroidal particles in Couette flows. *J. Fluid Mech.* 692, 369–394.
- Jeffery, G.B., 1922. The motion of ellipsoidal particles immersed in a viscous fluid. *Proc. R. Soc. Lond. Ser. A* 102, 161–179.
- Jones, W.P., di Mare, F., Marquis, A.J., 2002. LES-BOFFIN: Users guide, technical memorandum. Mechanical Engineering Department, Imperial College of Science, Technology and Medicine, London, UK.
- Karnis, A., Goldsmith, H.L., Mason, S.G., 1963. Axial migration of particles in Poiseuille flow. *Nature* 200, 159–160.
- Karnis, A., Goldsmith, H.L., Mason, S.G., 1966. The flow of suspensions through tubes: V. Inertial effects. *Can. J. Chem. Eng.* 44, 181–193.
- Kershaw, D.S., 1978. The incomplete Cholesky-conjugate gradient method for the iterative solution of systems of linear equations. *J. Comput. Phys.* 26, 43–65.
- Lilly, D.K., 1967. The representation of small-scale turbulence in numerical simulation experiments. In: Proceedings of the IBM Scientific Computing Symposium on Environmental Sciences, IBM Data Processing Division. White Plains, New York, pp. 195–210.
- Loth, E., 2008. Drag of non-spherical solid particles of regular and irregular shape. *Powder Technol.* 182, 342–353.
- Mando, M., Rosendahl, L., 2010. On the motion of non-spherical particles at high Reynolds number. *Powder Technol.* 202, 1–13.
- Marchioli, C., Fantoni, M., Soldati, A., 2010. Orientation, distribution, and deposition of elongated, inertial fibers in turbulent channel flow. *Phys. Fluids* 22, 033301–033314.
- Marchioli, C., Soldati, A., 2007. Reynolds number scaling of particle preferential concentration in turbulent channel flow. In: Palma, J.M.L.M., Lopes, A.S. (Eds.), *Advances in Turbulence XI*. Springer, Berlin Heidelberg, pp. 298–300.
- Marchioli, C., Soldati, A., 2013. Rotation statistics of fibers in wall shear turbulence. *Acta Mech.* 224, 2311–2329.
- Marchioli, C., Soldati, A., Kuerten, J.G.M., Arcen, B., Tanière, A., Goldensoph, G., Squires, K.D., Cargnelutti, M.F., Portela, L.M., 2008. Statistics of particle dispersion in direct numerical simulations of wall-bounded turbulence: results of an international collaborative benchmark test. *Int. J. Multiph. Flow* 34, 879–893.
- Mortensen, P.H., Andersson, H.I., Gillissen, J.J.J., Boersma, B.J., 2008a. Dynamics of prolate ellipsoidal particles in a turbulent channel flow. *Phys. Fluids* 20, 093302–093314.
- Mortensen, P.H., Andersson, H.I., Gillissen, J.J.J., Boersma, B.J., 2008b. On the orientation of ellipsoidal particles in a turbulent shear flow. *Int. J. Multiph. Flow* 34, 678–683.
- Njobuenwu, D.O., Fairweather, M., 2013a. Inertial particle behaviour in turbulent fluid flow. In: Andrzej, K., Ilkka, T. (Eds.), *Proceedings of the 23rd European Symposium on Computer Aided Process Engineering – ESCAPE 23*, 32 ed., Computer Aided Chemical Engineering, 32, Lappeenranta, Finland, pp. 253–258.
- Njobuenwu, D.O., Fairweather, M., 2013b. Non-spherical particle translation and orientation in wall-bounded turbulence. In: Simos, T.E., Psihogios, G., Tsitouras, C. (Eds.), *Proceedings of the 11th International Conference on Numerical Analysis and Applied Mathematics 2013 (ICNAAM-2013)*, Rhodes, Greece. AIP Conference Proceedings, vol. 1558, pp. 132–135.
- Njobuenwu, D.O., Fairweather, M., 2014. Effect of shape on inertial particle dynamics in a channel flow. *Flow Turbul. Combust.* 92, 83–101.
- Njobuenwu, D.O., Fairweather, M., Yao, J., 2013. Coupled RANS-LPT modelling of dilute, particle-laden flow in a duct with a 90° bend. *Int. J. Multiph. Flow* 50, 71–88.
- Pan, T.-W., Chang, C.-C., Glowinski, R., 2008. On the motion of a neutrally buoyant ellipsoid in a three-dimensional Poiseuille flow. *Comput. Methods Appl. Mech. Eng.* 197, 2198–2209.
- Pan, Y., Tanaka, T., Tsuji, Y., 2001. Direct numerical simulation of particle-laden rotating turbulent channel flow. *Phys. Fluids* 13, 2320–2337.
- Piomelli, U., Liu, J., 1995. Large-eddy simulation of rotating channel flows using a localized dynamic model. *Phys. Fluids* 7, 839–848.
- Port-Agel, F., Meneveau, C., Parlange, M.B., 2000. A scale-dependent dynamic model for large-eddy simulation: application to a neutral atmospheric boundary layer. *J. Fluid Mech.* 415, 261–284.
- Qi, D., Luo, L., 2002. Transitions in rotations of a nonspherical particle in a three-dimensional moderate Reynolds number Couette flow. *Phys. Fluids* 14, 4440–4443.
- Qi, D., Luo, L., 2003. Rotational and orientational behaviour of three-dimensional spheroidal particles in Couette flows. *J. Fluid Mech.* 477, 201–213.
- Rhie, C.M., Chow, W.L., 1983. Numerical study of the turbulent flow past an airfoil with trailing edge separation. *AIAA J.* 21, 1525–1532.
- Salmanzadeh, M., Rahnama, M., Ahmadi, G., 2010. Effect of sub-grid scales on large eddy simulation of particle deposition in a turbulent channel flow. *Aerosol Sci. Technol.* 44, 796–806.
- Shapiro, M., Goldenberg, M., 1993. Deposition of glass fiber particles from turbulent air flow in a pipe. *J. Aerosol Sci.* 24, 65–87.
- Swamee, P., Ojha, C., 1991. Drag coefficient and fall velocity of nonspherical particles. *J. Hydraul. Eng.* 117, 660–667.
- Tian, L., Ahmadi, G., Wang, Z., Hopke, P.K., 2012. Transport and deposition of ellipsoidal fibers in low Reynolds number flows. *J. Aerosol Sci.* 45, 1–18.
- van der Vorst, H., 1992. Bi-CGSTAB: a fast and smoothly converging variant of Bi-CG for the solution of nonsymmetric linear systems. *SIAM J. Sci. Statist. Comput.* 13, 631–644.
- Wang, Q., Squires, K.D., 1996a. Large eddy simulation of particle-laden turbulent channel flow. *Phys. Fluids* 8, 1207–1223.
- Wang, Q., Squires, K.D., 1996b. Large eddy simulation of particle deposition in a vertical turbulent channel flow. *Int. J. Multiph. Flow* 22, 667–683.
- Wang, Q., Squires, K.D., Chen, M., McLaughlin, J.B., 1997. On the role of the lift force in turbulence simulations of particle deposition. *Int. J. Multiph. Flow* 23, 749–763.
- Winkler, C.M., 2002. Large Eddy Simulations of Particle Dispersion and Deposition in a Turbulent Square Duct Flow. Mechanical and Industrial Engineering Department, University of Illinois at Urbana-Champaign, USA.
- Yin, C., Rosendahl, L., K. Kær, S., Condra, T., J., 2004. Use of numerical modeling in design for co-firing biomass in wall-fired burners. *Chem. Eng. Sci.* 59, 3281–3292.
- Yin, C., Rosendahl, L., Knudsen Kær, S., Sørensen, H., 2003. Modelling the motion of cylindrical particles in a nonuniform flow. *Chem. Eng. Sci.* 58, 3489–3498.
- Yu, Z., Phan-Thien, N., Tanner, R.I., 2007. Rotation of a spheroid in a Couette flow at moderate Reynolds numbers. *Phys. Rev. E* 76, 026310.
- Zastawny, M., Mallouppas, G., Zhao, F., van Wachem, B., 2012. Derivation of drag and lift force and torque coefficients for non-spherical particles in flows. *Int. J. Multiph. Flow* 39, 227–239.
- Zhang, H., Ahmadi, G., Fan, F.-G., McLaughlin, J.B., 2001. Ellipsoidal particles transport and deposition in turbulent channel flows. *Int. J. Multiph. Flow* 27, 971–1009.
- Zhao, L., Marchioli, C., Andersson, H.I., 2014. Slip velocity of rigid fibers in turbulent channel flow. *Phys. Fluids* (1994–present) 26, 063302 <http://dx.doi.org/10.1063/1.4881942>.
- Zhao, L.H., Marchioli, C., Andersson, H.I., 2012. Stokes number effects on particle slip velocity in wall-bounded turbulence and implications for dispersion models. *Phys. Fluids* 24, 021705–021707.